Computer Methods in Applied Mechanics and Engineering

A wavelet-enhanced adaptive hierarchical FFT-based approach for the efficient solution of microscale boundary value problems

--Manuscript Draft--

Manuscript Number:	
Article Type:	Research Paper
Keywords:	Computational Multiscale Methods; Spectral Solver; FFT; Wavelets; Adaptivity; Non-uniform Grid
Corresponding Author:	Tobias Kaiser, Dr.-Ing. Eindhoven University of Technology Eindhoven, NETHERLANDS
First Author:	Tobias Kaiser, Dr.
Order of Authors:	Tobias Kaiser, Dr.
	Thorsten Raasch, Prof.
	Joris J. C. Remmers, Associate Prof.
	Marc G. D. Geers, Prof.
Abstract:	This contribution focuses on the development of an adaptive hierarchical FFT-based approach for the efficient solution of microscale boundary value problems. To this end, the classic Moulinec-Suquet scheme is revisited and enhanced by making use of wavelet analysis. Governing fields are represented in a wavelet basis and higher level stress approximations in a nested set of approximation spaces are successively derived by making use of wavelet transforms. By adaptively refining the computational grid based on the solution profile, localised features can be resolved accurately while the overall number of material model evaluations is significantly reduced. The performance is demonstrated by a detailed study of representative boundary value problems in one- and two-dimensional domains, whereby a reduction in the number of material model evaluations of up to 95% has been achieved.
Suggested Reviewers:	Joaquin Alberto Hernandez Prof., International Center for Numerical Methods in Engineering jhortega@cimne.upc.edu
	Ali Javili Asst. Prof., Bilkent University ajavili@bilkent.edu.tr
	Marc-Andre Keip Prof., University of Stuttgart marc-andre.keip@mechbau.uni-stuttgart.de
	Xavier Oliver Prof., International Center for Numerical Methods in Engineering xavier.oliver@upc.edu
	Paul Steinmann Friedrich-Alexander University Erlangen-Nuremberg paul.steinmann@fau.de
	Julien Yvonnet Prof., Gustave Eiffel University julien.yvonnet@univ-eiffel.fr

Cover Letter

Dr.-Ing.
Tobias Kaiser

Tobias Kaiser · Mechanics of Materials, TU/e, Groene Loper · 5612 AZ Eindhoven

Mechanics of Materials, TU/e,
Groene Loper
5612 AZ Eindhoven

Phone +49 231 755 3567
Telefax +49 231 755 2688
e-mail:
t.kaiser@tue.nl

Computational Methods in Applied Mechanics and Engineering

28. November 2022

Manuscript for Computational Methods in Applied Mechanics and Engineering

Dear Editor,

Enclosed please find the manuscript '*A wavelet-enhanced adaptive hierarchical FFT-based approach for the efficient solution of microscale boundary value problems*' authored by Thorsten Raasch, Joris J. C. Remmers, Marc G. D. Geers and myself, which we would like to publish in Computational Methods in Applied Mechanics and Engineering.

As possible reviewers, amongst others, we propose:

* Prof. Joaquin Alberto Hernández, Centre Internacional de Métodes Numérics en Enginyeria, Universitat Politécnica de Catalunya, jhortega@cimne.upc.edu
* Asst. Prof. Ali Javili, Department of Mechanical Engineering, Bilkent University, ajavili@bilkent.edu.tr
* Prof. Marc-André Keip, Institute of Applied Mechanics, University of Stuttgart, marc-andre.keip@mechbau.uni-stuttgart.de
* Prof. Xavier Oliver, Centre Internacional de Métodes Numérics en Enginyeria, Universitat Politécnica de Catalunya, xavier.oliver@upc.edu
* Prof. Paul Steinmann, Institute of Applied Mechanics, Friedrich-Alexander-Universität Erlangen-Nürnberg, paul.steinmann@fau.de
* Prof. Julien Yvonnet, Multiscale Modelling and Simulation Laboratory, Gustave Eiffel University, Paris, julien.yvonnet@univ-eiffel.fr

Whereas it may seem natural to consider Prof. Karel Matous as a reviewer for this paper as well, it might be good for the editor to know that we collaborated with him on the subject of wavelet-based mechanics.

With many thanks for your effort and with kind regards I remain,

Yours sincerely,

Tobias Kaiser (Corresponding Author)

A wavelet-enhanced adaptive hierarchical FFT-based approach for the efficient solution of microscale boundary value problems

–

Highlights

- State of the art wavelet-enhanced FFT-based solution approach
- Adaptive grid refinement
- Significant reduction in number of material model evaluations
- Eshelby-Green operator for wavelet-based discretisations

A wavelet-enhanced adaptive hierarchical FFT-based approach for the efficient solution of microscale boundary value problems

Tobias Kaiser[a,b], Thorsten Raasch[c], Joris J. C. Remmers[a], Marc G. D. Geers[a]

[a]*Department of Mechanical Engineering, Eindhoven University of Technology, P.O. Box 513, 5600 MB Eindhoven, The Netherlands*
[b]*Department of Mechanical Engineering, Institute of Mechanics, TU Dortmund University, Leonhard-Euler-Str. 5, 44227 Dortmund, Germany*
[c]*Department of Mathematics, University of Siegen, Walter-Flex-Str. 3, 57068 Siegen, Germany*

Abstract

This contribution focuses on the development of an adaptive hierarchical FFT-based approach for the efficient solution of microscale boundary value problems. To this end, the classic Moulinec-Suquet scheme is revisited and enhanced by making use of wavelet analysis. Governing fields are represented in a wavelet basis and higher level stress approximations in a nested set of approximation spaces are successively derived by making use of wavelet transforms. By adaptively refining the computational grid based on the solution profile, localised features can be resolved accurately while the overall number of material model evaluations is significantly reduced. The performance is demonstrated by a detailed study of representative boundary value problems in one- and two-dimensional domains, whereby a reduction in the number of material model evaluations of up to 95% has been achieved.

Keywords: Continuum Mechanics, Computational Multiscale Methods, Computational Homogenisation, Spectral Solver, FFT, Wavelets, Adaptivity, Grid Refinement, Non-uniform Grid

1. Introduction

Computational homogenisation and multiscale methods are sophisticated approaches to predict the effective constitutive response of complex multiphase microstructures in numerical simulations. To this end, detailed information of the underlying microstructure is collected in representative volume elements (RVEs), for instance by geometrically resolving microscale features such as individual grains, fibres or voids, and by taking sophisticated constitutive models into account that have been developed at the level of individual phases [1].

Originating from the pioneering works [2, 3], first-order multiscale approaches are meanwhile well-established in the continuum mechanics community to understand and predict the effective macroscale response of complex material systems. This includes purely mechanical [4, 5, 6, 7, 8, 9], thermo-mechanical [10, 11, 12, 13, 14], and electro-mechanical problems of electrical conductors [15, 16] and electro-active materials [17, 18, 19], respectively. However, the repetitive solution of microscale boundary value problems that substitutes the evaluation of closed-form constitutive models is associated with a significant increase in computational cost, both in terms of CPU-time and memory requirements. This is particularly problematic when considering non-linear history-dependent material behaviour, impeding the widespread application of computational multiscale methods.

Against this background, tailored solution techniques have been proposed that make use of the specific structure of the underlying microscale problem. The geometry of the computational cell may be chosen arbitrarily as long as it contains "sufficient" information to be statistically representative for the particular microstructure under consideration. For simplicity, these microscale boundary value problems are therefore generally formulated on rectangular domains without loss of generality. Moreover, the unit cells are typically subjected to periodic boundary conditions in a manner that is consistent with the Hill-Mandel energy equivalence condition, which has been shown to perform best in predicting effective properties compared with affine displacement and uniform traction boundary conditions [20].

Email addresses: tobias.kaiser@tu-dortmund.de (Tobias Kaiser), raasch@mathematik.uni-siegen.de (Thorsten Raasch), j.j.c.remmers@tue.nl (Joris J. C. Remmers), m.g.d.geers@tue.nl (Marc G. D. Geers)

Motivated by the specific structure of the microscale boundary value problem, FFT-based solution approaches have been the focus of intense research, see [21, 22] for detailed reviews. These approaches originate from the pioneering works [23, 24, 25] and rely on Fourier space representations of the governing fields and the Eshelby-Green operator. More specifically, the microscale boundary value problem is reformulated as an integral equation that can efficiently be evaluated in Fourier space and use is made of sophisticated implementations of the fast Fourier transform (FFT) [26, 27] to map field quantities from the physical to the frequency space and vice versa. Being developed for general, non-linear microscale material models, the so-called basic scheme proposed by Moulinec-Suquet stipulates a fixed-point-type update procedure for the fluctuation strains [23, 24, 25]. However, the basic scheme is rather slow compared to state of the art solution techniques [28, 21]. In particular, it is observed that the convergence rate significantly depends on the material contrast and on the chosen reference material which resembles a tensor-valued numerical tuning constant. Properly choosing the reference material for complex evolving microstructures that exhibit non-linear history-dependent material behaviour poses a challenge, and a poor choice results in a significant increase in computational costs. Likewise, the iteration count and hence the computational effort of the basic scheme becomes excessive for large phase contrasts [28, 21]. Furthermore, it is noted that the classic Moulinec-Suquet discretisation that manifests itself in the specific form of the Eshelby-Green operator is based on trigonometric polynomials which allow for spurious Gibbs-type oscillations to occur when the physical fields under consideration are not sufficiently smooth. Considering purely mechanical problems, this is typically the case when material interfaces, e.g. grain or phase boundaries, occur in the solution domain which, in general, induce weak-singularities in the displacement field. Finally, it is remarked that due to its reliance on efficient implementations of the fast Fourier transform, a regular structured grid is assumed. This is a significant restriction when small-scale features occur in the solution domain since the grid spacing is determined by the smallest feature to be resolved. Accordingly, the system size and the number of material model evaluations significantly increase.

To address the drawbacks of the basic scheme, different solution approaches with their own merits and limitations have been proposed [28, 21]. Consider for instance the conjugate gradient solver proposed in [29] that is fast but limited to linear problems, the polarisation schemes suggested in [30, 31] which are computationally efficient when applicable but exhibit only logarithmic convergence for infinite phase contrast, or the fast gradient method proposed in [32] that is efficient compared to the basic scheme but requires twice the memory and a proper choice of numerical tuning constants. Likewise, alternative discretisation schemes, different from the classic Moulinec-Suquet discretisation, have been proposed that increase the overall convergence rate, allow microstructures with infinite phase contrast to be considered or resolve the spurious oscillations of the Moulinec-Suquet discretisation, e.g. [33, 34, 35].

In the light of the developments for fast and efficient FFT-based solution approaches the recently proposed Barzilai-Borwein extended version of the basic scheme, cf. [28], which does not depend on numerical tuning constants, which is not limited to linear relations and which is capable of treating microstructures with infinite phase contrasts, is adopted in this work. The scheme is based on the interpretation of the basic scheme as a gradient descent method and makes use of the well-established Barzilai-Borwein step size selection to be competitive with the fastest solvers available. Addressing the regular grid spacing and the associated number of material model evaluations, the scheme is extended in the present contribution by taking into account a wavelet-based discretisation. In this regard, the multiresolution properties of wavelets are the key to construct an adaptive hierarchical FFT-based approach that allows localised microscale features to be properly resolved while maintaining a rather coarse discretisation in the rest of the solution domain. Regarding the irregular grid spacing, it is noted that the present approach shares similarities with non-uniform fast Fourier transforms (NUFFTs) that allow for an efficient approximation of the discrete Fourier transform (DFT) when using a reduced set of non-uniformly distributed sampling points. Similar to NUFFT approaches, the function under consideration is only evaluated at certain selected grid points in the present approach. These are determined by making use of the intrinsic adaptivity of wavelet-based approaches, whereas use is made of the "classic" FFT approach (unlike NUFFT) on the wavelet approximation of the respective function on the underlying regular grid. To the authors best knowledge and in accordance with [36], it is observed that NUFFT-appraoches have not yet been studied in the context of microscale boundary value problems. In addition, it is shown that the gain in computational efficiency of the proposed wavelet-based approach depends on the particular form of the Eshelby-Green operator and that a significant (additional) gain can be achieved by replacing the Eshelby-Green operator associated with a Moulinec-Suquet discretisation with one that is consistent with the underlying wavelet discretisation.

Wavelet analysis has emerged in the early 1980s, driven by applications in seismic geology [37], electrical engineering [38] and quantum science [39]. It is based on the fundamental concept of multiresolution analysis [40]

and has been shown to be particularly useful in the study of physics problems that include characteristic features at distinct length scales. Hence, it is often also referred to as the numerical microscope [41]. By providing a hierarchical sequence of basis functions and by establishing transformation relations between the different resolution levels considered, wavelet-based approaches allow signals to be systematically analysed and compressed by successively "peeling off" high frequency components. Vice versa, compressed signals may be retrieved and detailed representations of a signal may be reconstructed by making use of wavelet synthesis operations. In this regard, wavelet-based approaches differ significantly from classic spectral approaches since wavelet basis functions have intrinsically good localisation properties in both physical and spectral space. This allows to determine the frequency spectrum of a signal and the locations in physical space at which particular frequencies occur [42], and to properly resolve localised features of a signal by systematically adding/removing higher level wavelets in the respective wavelet expansion. Due to their remarkable time-frequency decomposition characteristics, adaptive wavelet-based approaches for the solution of (partial) differential equations have been subject of intense research, see [41] for a detailed review. These include wavelet collocation [43, 44, 45], wavelet Galerkin [46, 47, 48] and wavelet finite element methods [49]. However, applications to continuum mechanics problems have been rather limited and there are only few works that focus for instance on the application of wavelets to structural optimisation problems [50] and the modelling of damage propagation [51], on wavelet-enhanced finite element-based approaches for the efficient solution of microscale boundary value problems [52, 53] or on adaptive wavelet-based reduced order models [54, 55].

Motivated by the promising properties of wavelet-based approaches in resolving localised features in the solution profile, the present contribution focuses on the research question "*Can adaptive hierarchical wavelet approaches be used to increase the computational efficiency of FFT-based spectral solvers for microscale boundary value problems?*", with the main contributions being:

- The development of an adaptive hierarchical FFT-based approach for the efficient solution of microscale boundary value problems that makes use of the multiresolution properties of wavelet discretisations and allows for localised microscale features to be accurately resolved while maintaining a rather coarse discretisation in the rest of the solution domain.
- The derivation of the specific explicit form of the Eshelby-Green operator in Fourier space, which is consistent with the wavelet discretisation of the field variables.

The contribution is structured as follows: The fundamentals of wavelet analysis as a basis for the adaptive hierarchical scheme to be developed are briefly recapitulated in Section 2. With these at hand, the classic FFT-based Moulinec-Suquet solution approach to microscale boundary value problems is revisited in Section 3 and a particular form of the Eshelby-Green operator that takes the underlying wavelet discretisation into account is derived. Section 4 addresses the combination of wavelet- and FFT-based spectral approaches before representative boundary value problems in one- and two-dimensional settings are studied in Section 5. The findings are summarised and concluding remarks are drawn in Section 6.

1.1. Notations

Throughout the paper, we consistently use the following notation conventions. Let scalars be denoted by α, first order tensors by $\vec{\alpha}$, second order tensors by $\boldsymbol{\alpha}$, vector-valued lists by $\underline{\alpha}$, matrix-valued list by $\underline{\underline{\alpha}}$, and let $\otimes$ denote the classic dyadic product. With these definitions at hand, single and double tensor contractions take the form $\left[\vec{\alpha}\otimes\vec{\beta}\right]\cdot\left[\vec{\gamma}\otimes\vec{\delta}\right] = \left[\vec{\beta}\cdot\vec{\gamma}\right]\left[\vec{\alpha}\otimes\vec{\delta}\right]$ and $\left[\vec{\alpha}\otimes\vec{\beta}\right] : \left[\vec{\gamma}\otimes\vec{\delta}\right] = \left[\vec{\alpha}\cdot\vec{\delta}\right]\left[\vec{\beta}\cdot\vec{\gamma}\right]$, and the non-standard dyadic products $\overline{\otimes}$ and $\underline{\otimes}$ are defined as $\left[\vec{\alpha}\otimes\vec{\beta}\right]\overline{\otimes}\left[\vec{\gamma}\otimes\vec{\delta}\right] = [\vec{\alpha}\otimes\vec{\gamma}]\otimes\left[\vec{\beta}\otimes\vec{\delta}\right]$ and $\left[\vec{\alpha}\otimes\vec{\beta}\right]\underline{\otimes}\left[\vec{\gamma}\otimes\vec{\delta}\right] = [\vec{\alpha}\otimes\vec{\gamma}]\otimes\left[\vec{\delta}\otimes\vec{\beta}\right]$. The volume average of a tensor-valued function on domain $\mathcal{B}$ is

$$\langle\boldsymbol{\alpha}\rangle = \frac{1}{\mathrm{vol}\,(\mathcal{B})}\int_{\mathcal{B}}\boldsymbol{\alpha}\,(\vec{x})\;\mathrm{d}v \quad , \tag{1}$$

the L^2-type inner product reads

$$\langle\boldsymbol{\alpha},\boldsymbol{\beta}\rangle_{L^2} = \frac{1}{\mathrm{vol}\,(\mathcal{B})}\int_{\mathcal{B}}\boldsymbol{\alpha}\,(\vec{x}) : \boldsymbol{\beta}^{\mathrm{t}}\,(\vec{x})\;\mathrm{d}v \quad , \tag{2}$$

and the L^2-type norm follows as

$$\|\boldsymbol{\alpha}\|_{L^2}^2 = \frac{1}{\mathrm{vol}\,(\mathcal{B})} \int_{\mathcal{B}} \boldsymbol{\alpha}\,(\vec{x}) : \boldsymbol{\alpha}^{\mathrm{t}}\,(\vec{x})\ \mathrm{d}v \quad . \tag{3}$$

Moreover, basis vectors $\vec{e}_i, i \in \{1, 2, 3\}$, refer to a Cartesian basis, $\boldsymbol{I}$ is the second order identity tensor and $\nabla\bullet$, $\nabla^{\mathrm{sym}}\bullet$, and $\nabla \cdot \bullet$ indicate (right-)gradient, symmetrised (right-)gradient and (right-)divergence operations, respectively.

2. Wavelets

This section focuses on the fundamentals of wavelet analysis and provides the basis for the development of the adaptive hierarchical FFT-based solution approach in Section 4. Against this background, focus lies on a one-dimensional setting in Section 2.1 before the general two-dimensional setting is discussed in Section 2.2. More thorough introductions to wavelet analysis are for instance provided in text books [56, 57, 58, 59].

2.1. One-dimensional wavelet analysis

Wavelet analysis is based on the fundamental framework of multiresolution analysis and offers a systematic hierarchical approach to analyse and approximate functions on different resolution levels. To this end, sequences of nested approximation spaces $\left\{\mathcal{V}^j : j \in \mathbb{Z}\right\}$ and detail spaces $\left\{\mathcal{W}^j : j \in \mathbb{Z}\right\}$ with $\mathcal{V}^{j+1} = \mathcal{V}^j \oplus \mathcal{W}^j$ are introduced. Moreover, it is required that a given function $f\,(x) : \mathbb{R} \to \mathbb{R}$ in $\mathcal{V}^0$ is related to its integer translates according to $f\,(x) \in \mathcal{V}^0 \Leftrightarrow f\,(x-k) \in \mathcal{V}^0\ \forall\, k \in \mathbb{Z}$ and that binary dilates belong to higher resolution levels according to $f\,(x) \in \mathcal{V}^0 \Leftrightarrow f\left(2^j x\right) \in \mathcal{V}^j\ \forall\, j \in \mathbb{Z}$. The approximation spaces are spanned by scaling functions $\left\{\phi_k^j : k \in \mathbb{Z}\right\}$, whereas functions $\left\{\psi_k^j : k \in \mathbb{Z}\right\}$ that span the detail spaces are referred to as wavelets. It can be shown that scaling functions and wavelets are related to mother scaling functions and mother wavelets according to

$$\phi_k^j\,(x) = \phi\left(2^j x - k\right) \quad , \tag{4a}$$

$$\psi_k^j\,(x) = \psi\left(2^j x - k\right) \quad , \tag{4b}$$

and that the refinement relations

$$\phi_k^j\,(x) = \sum_l h_l\, \phi_{2k+l}^{j+1}\,(x) \quad , \tag{5a}$$

$$\psi_k^j\,(x) = \sum_l g_l\, \phi_{2k+l}^{j+1}\,(x) \quad , \tag{5b}$$

hold. Furthermore, it is observed that the filter coefficients h_l and g_l that appear in (5) uniquely define a particular biorthogonal wavelet family together with the filter coefficients $\tilde{h}_l$ and $\tilde{g}_l$ that characterise the dual scaling functions

$$\tilde{\phi}_k^j\,(x) = 2^j\, \tilde{\phi}\left(2^j x - k\right) \quad , \quad \tilde{\phi}_k^j\,(x) = \sum_l \tilde{h}_l\, \tilde{\phi}_{2k+l}^{j+1}\,(x) \quad , \tag{6}$$

and the dual wavelets

$$\tilde{\psi}_k^j\,(x) = 2^j\, \tilde{\psi}\left(2^j x - k\right) \quad , \quad \tilde{\psi}_k^j\,(x) = \sum_l \tilde{g}_l\, \tilde{\phi}_{2k+l}^{j+1}\,(x) \quad , \tag{7}$$

respectively, [57, 60].

In this contribution, Deslauriers-Dubuc wavelets [61] will be used. This wavelet family can be derived by means of successive polynomial interpolation between $2N$ support points. The Deslauriers-Dubuc mother scaling function $\phi\,(x)$ is interpolating in the sense $\phi\,(k) = \delta_{0k}\ \forall\, k \in \mathbb{Z}$, has compact support $\mathrm{supp}\,(\phi) = [-2N+1,\ 2N-1]$ and it can be shown that polynomials up to degree $2N-1$ can exactly be reproduced by linear combinations of $\phi_k^j\,(x)$, see [43]. For the particular choice $N = 2$ the filter coefficients are exemplarily provided in Table 1 and the mother scaling function and wavelet are depicted in Figure 1. Their dual counterparts are not shown since they are defined in terms of delta

distributions according to $\tilde{\phi}_{N=2}(x) = \delta(x)$ and $\tilde{\psi}_{N=2}(x) = \frac{1}{32}\delta(x-2) - \frac{9}{32}\delta(x-1) + \frac{1}{2}\delta\left(x-\frac{1}{2}\right) - \frac{9}{32}\delta(x) + \frac{1}{32}\delta(x+1)$. In virtue of (5), it is noted that the Deslauriers-Dubuc wavelet is a scaled and translated version of the corresponding scaling function, namely $\psi(x) = 2\,\phi(2\,x-1)$.

With the nested approximation spaces $\mathcal{V}^j$ at hand, a function $f(x)$ may be approximated on different resolution levels j according to

$$f(x) \approx f^j(x) = \sum_k s_k^j\,\phi_k^j(x) = \sum_k s_k^0\,\phi_k^0(x) + \sum_{i=0}^{j-1}\sum_k d_k^i\,\psi_k^i(x) \tag{8}$$

where s_k^j and d_k^i denote the scaling function and wavelet coefficients, respectively. Regarding (8), a representation that is only based on scaling functions is referred to as a scaling function representation of function $f(x)$, whereas a representation both in terms of scaling functions and wavelets will be referred to as a wavelet representation. By dropping wavelet coefficients smaller than a preset tolerance ϵ_d in the wavelet representation, the function may be represented in a compressed form as

$$f^j(x) \approx f_{\geq}^j(x) = \sum_k s_k^0\,\phi_k^0(x) + \sum_{i=0}^{j-1}\sum_{\substack{k \\ |d_k^i| \geq \epsilon_d}} d_k^i\,\psi_k^i(x) \tag{9}$$

where higher-level wavelets are only activated when necessary. This is demonstrated in Figure 2 in terms of a wavelet-discretised periodised Gaussian.

Due to the hierarchical character of the multiresolution analysis, the scaling function and wavelet coefficients on different resolution levels are not independent but can be related to one another by making use of wavelet analysis (forward wavelet transform)

$$s_k^j = \sum_l \tilde{h}_l\,s_{2k+l}^{j+1} \quad , \tag{10a}$$

$$d_k^j = \sum_l \tilde{g}_l\,s_{2k+l}^{j+1} \quad , \tag{10b}$$

and wavelet synthesis (backward wavelet transform)

$$s_{2k}^{j+1} = \sum_l h_{2l}\,s_{k-l}^j + \sum_l g_{2l}\,d_{k-l}^j \quad , \tag{11a}$$

$$s_{2k+1}^{j+1} = \sum_l h_{2l+1}\,s_{k-l}^j + \sum_l g_{2l+1}\,d_{k-l}^j \quad , \tag{11b}$$

operations. The linear set of relations (10) and (11) can be compacted in a vector-matrix multiplication form according to

$$\begin{bmatrix} \underline{s}^j \\ \underline{d}^j \end{bmatrix} = \underline{\underline{F}}_{j+1}^j\,\underline{s}^{j+1} \quad , \qquad \underline{s}^{j+1} = \underline{\underline{B}}_j^{j+1}\begin{bmatrix} \underline{s}^j \\ \underline{d}^j \end{bmatrix} \quad . \tag{12}$$

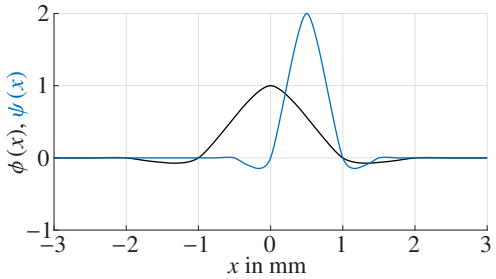

Figure 1: Deslauriers-Dubuc scaling function and wavelet ($N = 2$).

l	-4	-3	-2	-1	0	1	2	3	4
h_l	0	$-\frac{1}{16}$	0	$\frac{9}{16}$	1	$\frac{9}{16}$	0	$-\frac{1}{16}$	0
g_l	0	0	0	0	0	2	0	0	0
$\tilde{h}_l$	0	0	0	0	1	0	0	0	0
$\tilde{g}_l$	0	0	$\frac{1}{32}$	0	$-\frac{9}{32}$	$\frac{1}{2}$	$-\frac{9}{32}$	0	$\frac{1}{32}$
c_l	0	0	$\frac{1}{12}$	$-\frac{2}{3}$	0	$\frac{2}{3}$	$-\frac{1}{12}$	0	0

Table 1: Filter coefficients of Deslauriers-Dubuc wavelets ($N = 2$).

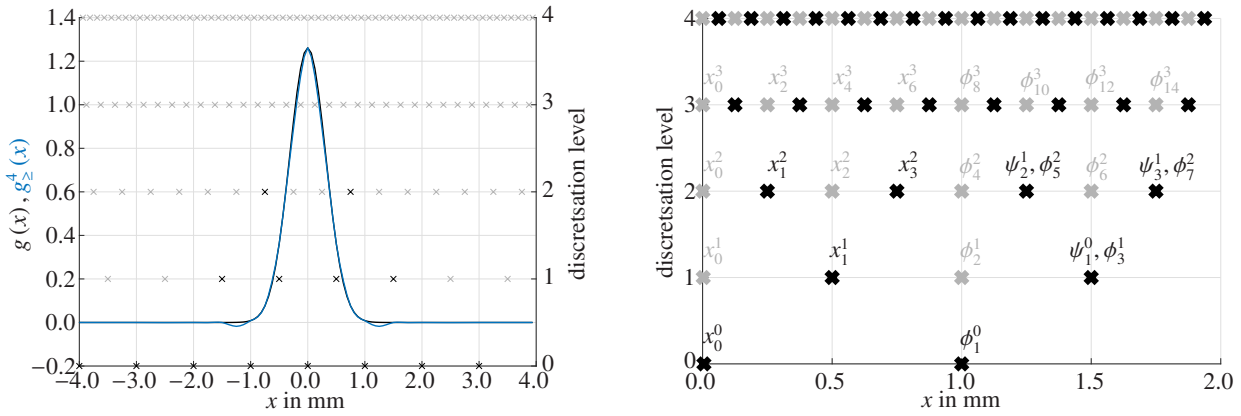

(a) wavelet expansion of Gaussian

(b) numbering of grid points and basis functions

Figure 2: Exemplary wavelet expansion and numbering of grid points and basis functions. a) One-dimensional periodised Gaussian $g(x) = [0.2 * \pi]^{-0.5} \exp\left(-5x^2\right)$ with period 8 and level 4 wavelet expansion $g_{\geq}^{4}(x)$ using Deslauriers-Dubuc wavelets ($N = 2$, $\epsilon_d = 0.025$). Active grid points are indicated in black colour, inactive grid points in grey colour. b) Numbering of grid points and basis functions. Black colour is used for grid points at the discretisation level where they occur for the first time, grey colour otherwise.

In view of (11) and by making use of $\tilde{\phi}_{N=2}(x) = \delta(x)$ it is moreover observed that

$$f\left(x_{2k}^{j+1}\right) = s_{2k}^{j+1} = s_k^j = f\left(x_k^j\right) \tag{13}$$

and

$$\begin{aligned} f\left(x_{2k+1}^{j+1}\right) = s_{2k+1}^{j+1} &= -\frac{1}{16}\, s_{k+2}^j + \frac{9}{16}\, s_{k+1}^j + \frac{9}{16}\, s_k^j - \frac{1}{16}\, s_{k-1}^j + 2\, d_k^j \\ &= -\frac{1}{16}\, f\left(x_{k+2}^j\right) + \frac{9}{16}\, f\left(x_{k+1}^j\right) + \frac{9}{16}\, f\left(x_k^j\right) - \frac{1}{16}\, f\left(x_{k-1}^j\right) + 2\, d_k^j \end{aligned} \quad , \tag{14}$$

hold, for the Deslauriers-Dubuc wavelet family defined by the filter coefficients provided in Table 1. Relation (13) implies that adding higher level wavelet contributions to the wavelet series (8) does not change the function values at lower level grid points. Likewise, regarding (14), it is observed that the wavelet coefficients d_k^j contain the missing data that is required to pass from a level j to a level $j+1$ representation of function $f(x)$ and, in particular, to correct the interpolation error at grid point x_{2k+1}^{j+1}.

In order to calculate derivatives of wavelet-discretised functions, the derivative filter coefficients

$$c_k = \int_{\mathcal{B}} \tilde{\phi}(x)\, \frac{\mathrm{d}}{\mathrm{d}x} \left(\phi(x-k)\right) \mathrm{d}x \tag{15}$$

are introduced. By making use of the refinement relations (5a) and (6), definition (15) stipulates an eigenvalue problem from which the unknown derivative filter coefficients can be determined, see [57, 60]. The resulting filter coefficients for the Deslauriers-Dubuc wavelet family with $N = 2$ on a regular grid with grid spacing $\eta = 1$ are provided in Table 1. By additionally invoking (4a) and (6), it is moreover observed that

$$\frac{c_{k-l}}{\eta^j} = \int_{\mathcal{B}} \tilde{\phi}_l^j(x)\, \frac{\mathrm{d}}{\mathrm{d}x} \left(\phi_k^j(x)\right) \mathrm{d}x \quad , \quad \eta^j = x_{k+1}^j - x_k^j \quad , \tag{16}$$

holds, which essentially adopts the filter to the grid-spacing η^j at resolution level j. With (16) at hand, taking the derivative of scaling function representation (8) and inserting (16) into the ensuing equation eventually results in

$$\left.\frac{\mathrm{d}f^j(x)}{\mathrm{d}x}\right|_{x=x_l^j} = \int_{\mathcal{B}} \tilde{\phi}_l^j(x)\, \frac{\mathrm{d}}{\mathrm{d}x} \left(\sum_k s_k^j\, \phi_k^j(x)\right) \mathrm{d}x = \sum_k \frac{c_{k-l}}{\eta^j}\, s_k^j = \sum_k \frac{c_k}{\eta^j}\, s_{k+l}^j \quad . \tag{17}$$

Finally, it is remarked that periodicity constraints on the function $f(x)$ can be accounted for by wrapping around indices that are out of bounds in all filter based operations, see [57, 60].

2.2. Two-dimensional wavelet analysis

The theoretical foundations presented in Section 2.1 can be generalised to a two-dimensional setting by making use of a tensor product ansatz. To this end, a set of grid points at spatial positions

$$\vec{x}^{\,j}_{k;l} = [x_1]^j_k \; \vec{e}_1 + [x_2]^j_l \; \vec{e}_2 \tag{18}$$

is introduced that constitutes an hierarchical two-dimensional grid. In analogy with the one-dimensional setting, each grid point is associated with a certain resolution level and (possibly multiple) basis functions, see Figure 3. In a two-dimensional setting, the four different types of basis functions

$${}^0Z^j_{k;l}(\vec{x}) = \phi^j_k(x_1)\;\phi^j_l(x_2) \quad , \tag{19a}$$

$${}^1Z^j_{k;l}(\vec{x}) = \phi^j_k(x_1)\;\psi^j_l(x_2) \quad , \tag{19b}$$

$${}^2Z^j_{k;l}(\vec{x}) = \psi^j_k(x_1)\;\phi^j_l(x_2) \quad , \tag{19c}$$

$${}^3Z^j_{k;l}(\vec{x}) = \psi^j_k(x_1)\;\psi^j_l(x_2) \quad , \tag{19d}$$

exist. Whereas the two-dimensional scaling function spaces consist of functions ${}^0Z^j_{k;l}(\vec{x})$, three different types of wavelets occur at each resolution level, namely, ${}^1Z^j_{k;l}(\vec{x})$, ${}^2Z^j_{k;l}(\vec{x})$, and ${}^3Z^j_{k;l}(\vec{x})$.

Similar to the one-dimensional setting, a scalar-valued function $f(\vec{x})$ can be expressed by using a scaling function or wavelet representation on different resolution levels

$$f^j(\vec{x}) = \sum_k \sum_l {}^0S^j_{k;l}\,{}^0Z^j_{k;l}(\vec{x}) = \sum_k \sum_l {}^0S^0_{k;l}\,{}^0Z^0_{k;l}(\vec{x}) + \sum_{i=0}^{j-1} \sum_k \sum_l \sum_{m=1}^{3} {}^mS^i_{k;l}\,{}^mZ^i_{k;l}(\vec{x}) \quad , \tag{20}$$

and approximations $f^j_{\geq}(\vec{x})$ can be derived by dropping scaling function coefficient ${}^mS^i_{k;l}, m \in \{1,2,3\}$ smaller than a prescribed tolerance ϵ_d.

Finally, by collecting the coefficients ${}^mS^j_{k;l}$ in matrices ${}^m\underline{\underline{S}}^j$ and by successively applying (12) to each dimension one arrives at a two-dimensional matrix-representation of the forward wavelet transform

$$\begin{bmatrix} {}^0\underline{\underline{S}}^j & {}^1\underline{\underline{S}}^j \\ {}^2\underline{\underline{S}}^j & {}^3\underline{\underline{S}}^j \end{bmatrix} = \underline{\underline{F}}^j_{j+1}\;\; {}^0\underline{\underline{S}}^{j+1}\;\; \left[\underline{\underline{F}}^j_{j+1}\right]^{\mathrm{t}} \tag{21}$$

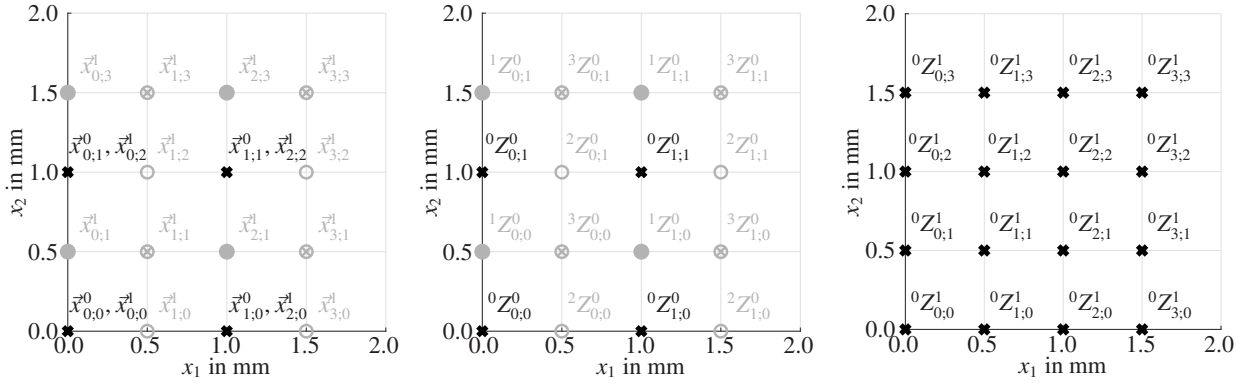

(a) level 0 and level 1 grid point numbering (b) level 0 basis function numbering (c) level 1 basis function numbering

Figure 3: Numbering of grid points and basis functions in a two-dimensional setting. a) Hierarchical grid featuring 2×2 grid points at discretisation level 0 and 4×4 grid points at discretisation level 1. Black colour is used for level 0 grid points, grey colour for grid points that occur the first time on discretisation level 1. b) Numbering of level 0 basis functions. Grid points associated with type 0 basis function are marked with ×, whereas •, ∘, and ⊗-symbols are used for type 1, type 2, and type 3 basis functions, respectively. c) Numbering of level 1 basis functions.

and backward wavelet transform

$$\underline{\underline{{}^{0}S}}^{j+1} = \underline{\underline{B}}_{j}^{j+1} \begin{bmatrix} \underline{\underline{{}^{0}S}}^{j} & \underline{\underline{{}^{1}S}}^{j} \\ \underline{\underline{{}^{2}S}}^{j} & \underline{\underline{{}^{3}S}}^{j} \end{bmatrix} \left[\underline{\underline{B}}_{j}^{j+1} \right]^{\mathrm{t}} \tag{22}$$

in a two-dimensional setting. For presentation purposes and without loss of generality, it was tacitly assumed in (21) and (22) that the same number of grid points is used in both spatial directions, such that the same transformation matrices are multiplied from the left and right, respectively. Wavelet transformations in dimensions higher than two follow in analogy with the preceding relations by applying the one-dimensional wavelet transformation to each dimension.

3. (FFT-based) spectral approach

This section focuses on the fundamentals of FFT-based spectral solvers. In particular, the derivation of the Moulinec-Suquet basic scheme that relies on a discretisation by means trigonometric functions, and of the associated Eshelby-Green operator, are briefly recapitulated in Section 3.1. Based on these derivations, Section 3.2 focuses on the derivation of the Eshelby-Green operator that is associated with a wavelet-based discretisation of the field variables. State of the art stabilisation schemes that significantly increase the convergence rate of the basic scheme are summarised in Section 3.3 and the convergence criterion adopted is discussed in Section 3.4.

3.1. Eshelby-Green operator and basic scheme

In the seminal works [23, 24, 25] a solution approach for microscale boundary value problems has been proposed that relies on Fourier space representations of the governing fields and solution operators, and that builds the basis for state of the art solution techniques. Microscale boundary value problems with periodic boundary conditions of the form

$$\nabla \cdot \boldsymbol{\sigma}(\vec{x}) = \vec{0} \;\; \forall \;\; \vec{x} \in \mathcal{B} \quad , \quad \vec{\omega}(\vec{x}^{-}) = \vec{\omega}(\vec{x}^{+}) \quad , \quad \boldsymbol{\sigma}(\vec{x}^{-}) \cdot \vec{n}(\vec{x}^{-}) = -\boldsymbol{\sigma}(\vec{x}^{+}) \cdot \vec{n}(\vec{x}^{-}) \quad , \tag{23}$$

are considered, where $\vec{x}^{-}$ and $\vec{x}^{+}$ denote points at opposing parts of the boundary $\partial\mathcal{B}$, see Figure 4. Based on thermodynamic considerations, the stresses $\boldsymbol{\sigma}(\vec{x})$ at each material point $\vec{x}$ of body $\mathcal{B}$ are assumed to be a function of strains $\boldsymbol{\varepsilon}(\vec{x})$, material parameters and, possibly, internal variables that characterise the material state. The governing potential of the strain field is the displacement field

$$\vec{u}(\vec{x}) = \vec{\omega}(\vec{x}) + \boldsymbol{\varepsilon}_{\mathrm{M}} \cdot \vec{x} \tag{24}$$

that is additively decomposed in an affine part in terms of macroscale strains $\boldsymbol{\varepsilon}_{\mathrm{M}}$ and a fluctuation part $\vec{\omega}(\vec{x})$. With (24) at hand the strain field takes the form

$$\boldsymbol{\varepsilon}(\vec{x}) = \boldsymbol{\varepsilon}^{*}(\vec{x}) + \boldsymbol{\varepsilon}_{\mathrm{M}} = \nabla^{\mathrm{sym}} \vec{u}(\vec{x}) \quad , \quad \boldsymbol{\varepsilon}^{*}(\vec{x}) = \nabla^{\mathrm{sym}} \vec{\omega}(\vec{x}) \quad , \quad \boldsymbol{\varepsilon}_{\mathrm{M}} = \langle \boldsymbol{\varepsilon}(\vec{x}) \rangle \quad . \tag{25}$$

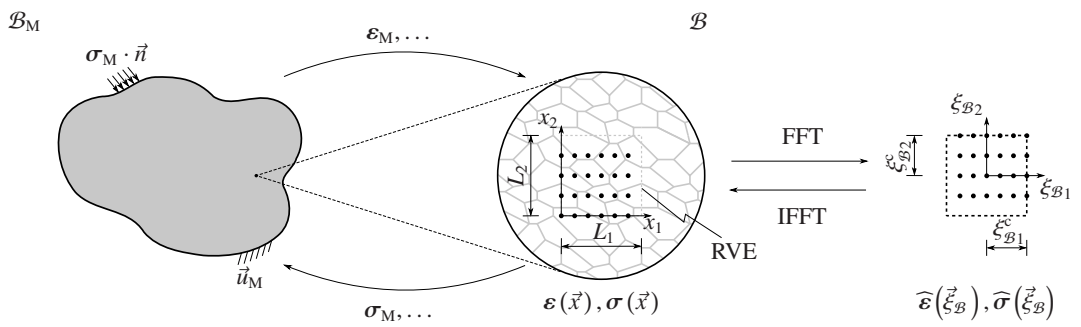

Figure 4: FFT-based solution approach for a periodic microscale boundary value problem.

By introducing polarisation stresses

$$\boldsymbol{\tau}(\vec{x}) = \boldsymbol{\sigma}(\vec{x}) - \mathbf{E}^0 : \boldsymbol{\varepsilon}^*(\vec{x}) \tag{26}$$

that correspond to a reference material with fourth order stiffness tensor $\mathbf{E}^0$, (23) gives rise to the Lippmann-Schwinger-type equations

$$\widehat{\boldsymbol{\varepsilon}}\left(\vec{\xi}_{\mathcal{B}}\right) = -\widehat{\boldsymbol{\Gamma}^0}\left(\vec{\xi}_{\mathcal{B}}\right) : \widehat{\boldsymbol{\tau}}\left(\vec{\xi}_{\mathcal{B}}\right) \;\forall\; \vec{\xi}_{\mathcal{B}} \neq \vec{0} \quad , \quad \widehat{\boldsymbol{\varepsilon}}\left(\vec{0}\right) = \boldsymbol{\varepsilon}_{\mathrm{M}} \tag{27a}$$

$$\boldsymbol{\varepsilon}(\vec{x}) = -\boldsymbol{\Gamma}^0\left(\boldsymbol{\tau}(\vec{x})\right) + \boldsymbol{\varepsilon}_{\mathrm{M}} \;\forall\; \vec{x} \in \mathcal{B} \tag{27b}$$

where $\widehat{\bullet}$ indicates the Fourier coefficients of the field variable $\bullet$ at angular frequencies $\vec{\xi}_{\mathcal{B}}$. Moreover, by inserting (26) into (27) and by observing that

$$\boldsymbol{\varepsilon}^*(\vec{x}) = \boldsymbol{\Gamma}^0\left(\mathbf{E}^0 : \boldsymbol{\varepsilon}^*(\vec{x})\right) \quad , \tag{28}$$

holds, one arrives at the fixed-point-type basic scheme

$${}^{n+1}\boldsymbol{\varepsilon}(\vec{x}) = {}^{n}\boldsymbol{\varepsilon}(\vec{x}) - \boldsymbol{\Gamma}^0\left({}^{n}\boldsymbol{\sigma}(\vec{x})\right) \quad , \tag{29}$$

where superscript n and $n+1$ refer to the iteration, see [25] for a detailed derivation. In Fourier space, representations of the Eshelby-Green operator $\widehat{\boldsymbol{\Gamma}^0}\left(\vec{\xi}_{\mathcal{B}}\right)$ are available and its application reduces to tensor contractions. In particular, for the isotropic reference material

$$\mathbf{E}^0 = 2\mu^0\,\mathbf{I}^{\mathrm{sym}} \quad , \quad \mathbf{I}^{\mathrm{sym}} = \frac{1}{2}\left[\boldsymbol{I}\overline{\otimes}\boldsymbol{I} + \boldsymbol{I}\underline{\otimes}\boldsymbol{I}\right] \tag{30}$$

with Lamé constant μ^0, $\widehat{\boldsymbol{\Gamma}^0}\left(\vec{\xi}_{\mathcal{B}}\right)$ takes the form

$$\widehat{\boldsymbol{\Gamma}^0}\left(\vec{\xi}_{\mathcal{B}}\right) = \frac{1}{2\mu^0}\left[\frac{\boldsymbol{I}\overline{\otimes}\left[\vec{\xi}_{\mathcal{B}}\otimes\vec{\xi}_{\mathcal{B}}\right] + \boldsymbol{I}\underline{\otimes}\left[\vec{\xi}_{\mathcal{B}}\otimes\vec{\xi}_{\mathcal{B}}\right] + \left[\vec{\xi}_{\mathcal{B}}\otimes\vec{\xi}_{\mathcal{B}}\right]\overline{\otimes}\boldsymbol{I} + \left[\vec{\xi}_{\mathcal{B}}\otimes\vec{\xi}_{\mathcal{B}}\right]\underline{\otimes}\boldsymbol{I}}{2\,\|\vec{\xi}_{\mathcal{B}}\|^2} - \frac{\vec{\xi}_{\mathcal{B}}\otimes\vec{\xi}_{\mathcal{B}}\otimes\vec{\xi}_{\mathcal{B}}\otimes\vec{\xi}_{\mathcal{B}}}{\|\vec{\xi}_{\mathcal{B}}\|^4}\right] \forall \vec{\xi}_{\mathcal{B}} \neq \vec{0}, \tag{31a}$$

$$\widehat{\boldsymbol{\Gamma}^0}\left(\vec{0}\right) = \mathbf{0} \quad . \tag{31b}$$

In a one-dimensional setting, (29) reduces to

$${}^{n+1}\varepsilon(x) = {}^{n}\varepsilon(x) - \Gamma^0\left({}^{n}\sigma(x)\right) \tag{32}$$

and the Eshelby-Green operator for a reference material with stiffness constant E^0 takes the form

$$\widehat{\Gamma^0}(\xi_{\mathcal{B}}) = \left[E^0\right]^{-1} \forall \xi_{\mathcal{B}} \neq 0 \quad , \quad \widehat{\Gamma^0}(0) = 0 \quad , \tag{33}$$

see Appendix A. In particular, it is observed that $\widehat{\Gamma^0}(\xi_{\mathcal{B}})$ is constant (except for the origin) and that $\widehat{\boldsymbol{\Gamma}^0}\left(\vec{\xi}_{\mathcal{B}}\right)$ is constant along lines in frequency space (except for the origin).

For rectangular RVEs that are in the focus of the present contribution, the frequency increments in Fourier space are determined by the RVE edge lengths L_i, see Figure 4. Likewise, the highest frequencies considered in the discrete Fourier transform (DFT) are related to the number of grid points in each spatial direction $\mathfrak{n}_i$ that are used in the discretisation of the microstructure. For an even number of grid points, the discrete frequency vectors take the form

$$\vec{\xi}_{\mathcal{B}} = \sum_i \xi_{\mathcal{B}i}\,\vec{\mathrm{e}}_i \quad , \quad \xi_{\mathcal{B}i} \in \left\{\xi_{\mathcal{B}i} \in \mathbb{R}\,|\,\xi_{\mathcal{B}i} = \frac{2\pi k}{L_i}, k \in \mathbb{Z}, -\frac{\mathfrak{n}_i}{2} < k \leq \frac{\mathfrak{n}_i}{2}\right\} \tag{34}$$

and care needs to be taken at the Nyquist frequencies ($\xi^{\mathrm{c}}_{\mathcal{B}i} = \frac{\pi\,\mathfrak{n}_i}{L_i}$ for some i) to ensure that the strain fields in (29) are real-valued, see the discussion in [24, 21]. In this contribution, the particular choice $\widehat{\boldsymbol{\Gamma}^0}\left(\xi_{\mathcal{B}1}, \xi^{\mathrm{c}}_{\mathcal{B}2}\right) = \widehat{\boldsymbol{\Gamma}^0}\left(\xi^{\mathrm{c}}_{\mathcal{B}1}, \xi_{\mathcal{B}2}\right) = \left[\mathbf{E}^0\right]^{-1}$ will be adopted that gives rise to real-valued strain updates in (29) and that forces the Fourier coefficients of the stress tensor (in the converged state) at the Nyquist frequencies to be zero.

3.2. Eshelby-Green operator for Deslauriers-Dubuc wavelet discretisations

In accordance with the developments of Eshelby-Green operators for discretisations based on finite difference schemes [34], the representation of the Eshelby-Green operator for a discretisation based on Deslauriers-Dubuc wavelets is derived in this section. In virtue of (17) and by using the symmetry properties of the derivative filter for the interpolating wavelets considered ($c_k = -c_{-k}$, $c_0 = 0$), it is observed that the gradient of the micro fluctuation field at discretisation level j,

$$\nabla\vec{\omega}^j(\vec{x}) = \sum_n \sum_k \frac{c_k}{\eta_n^j}\, \vec{\omega}\left(\vec{x} + k\,\eta_n^j\,\vec{e}_n\right) \otimes \vec{e}_n \quad , \tag{35}$$

has the Fourier space representation

$$\begin{aligned} \widehat{\nabla\vec{\omega}^j}\left(\vec{\xi}_{\mathcal{B}}\right) &= \sum_n \sum_k \frac{c_k}{\eta_n^j}\, \exp\left(\mathrm{i}\,k\,\eta_n^j\,\vec{\xi}_{\mathcal{B}}\cdot\vec{e}_n\right)\, \widehat{\vec{\omega}^j}\left(\vec{\xi}_{\mathcal{B}}\right)\otimes\vec{e}_n \\ &= \sum_n \sum_k \frac{c_k}{\eta_n^j}\, \left[\cos\left(k\,\eta_n^j\,\vec{\xi}_{\mathcal{B}}\cdot\vec{e}_n\right) + \mathrm{i}\,\sin\left(k\,\eta_n^j\,\vec{\xi}_{\mathcal{B}}\cdot\vec{e}_n\right)\right]\widehat{\vec{\omega}^j}\left(\vec{\xi}_{\mathcal{B}}\right)\otimes\vec{e}_n = \mathrm{i}\,\widehat{\vec{\omega}^j}\left(\vec{\xi}_{\mathcal{B}}\right)\otimes\vec{\beta}^j\left(\vec{\xi}_{\mathcal{B}}\right) \end{aligned} \tag{36}$$

with

$$\vec{\beta}^j\left(\vec{\xi}_{\mathcal{B}}\right) = \sum_n \sum_k \frac{c_k}{\eta_n^j}\, \sin\left(k\,\eta_n^j\,\vec{\xi}_{\mathcal{B}}\cdot\vec{e}_n\right)\,\vec{e}_n \quad . \tag{37}$$

Likewise, the divergence of the wavelet-discretised stress field at level j,

$$\nabla\cdot\boldsymbol{\sigma}^j(\vec{x}) = \sum_n \sum_k \frac{c_k}{\eta_n^j}\, \boldsymbol{\sigma}\left(\vec{x} + k\,\eta_n^j\,\vec{e}_n\right)\cdot\vec{e}_n \quad , \tag{38}$$

can be represented in Fourier space as

$$\begin{aligned} \widehat{\nabla\cdot\boldsymbol{\sigma}^j}\left(\vec{\xi}_{\mathcal{B}}\right) &= \sum_n \sum_k \frac{c_k}{\eta_n^j}\, \exp\left(\mathrm{i}\,k\,\eta_n^j\,\vec{\xi}_{\mathcal{B}}\cdot\vec{e}_n\right)\, \widehat{\boldsymbol{\sigma}^j}\left(\vec{\xi}_{\mathcal{B}}\right)\cdot\vec{e}_n \\ &= \sum_n \sum_k \frac{c_k}{\eta_n^j}\, \left[\cos\left(k\,\eta_n^j\,\vec{\xi}_{\mathcal{B}}\cdot\vec{e}_n\right) + \mathrm{i}\,\sin\left(k\,\eta_n^j\,\vec{\xi}_{\mathcal{B}}\cdot\vec{e}_n\right)\right]\widehat{\boldsymbol{\sigma}^j}\left(\vec{\xi}_{\mathcal{B}}\right)\cdot\vec{e}_n = \mathrm{i}\,\widehat{\boldsymbol{\sigma}^j}\left(\vec{\xi}_{\mathcal{B}}\right)\cdot\vec{\beta}^j\left(\vec{\xi}_{\mathcal{B}}\right) \end{aligned} \quad . \tag{39}$$

By making use of the structural similarity between the wavelet-based representations (36) and (39), and their analytical analogues

$$\widehat{\nabla\vec{\omega}}\left(\vec{\xi}_{\mathcal{B}}\right) = \mathrm{i}\,\widehat{\vec{\omega}}\left(\vec{\xi}_{\mathcal{B}}\right)\otimes\vec{\xi}_{\mathcal{B}} \quad , \tag{40a}$$

$$\widehat{\nabla\cdot\boldsymbol{\sigma}}\left(\vec{\xi}_{\mathcal{B}}\right) = \mathrm{i}\,\widehat{\boldsymbol{\sigma}}\left(\vec{\xi}_{\mathcal{B}}\right)\cdot\vec{\xi}_{\mathcal{B}} \quad , \tag{40b}$$

in the derivation of the Eshelby-Green operator, cf. [25], one eventually arrives at the Fourier space representation of the wavelet discretisation-based Eshelby-Green operator

$$\begin{aligned} \widehat{\boldsymbol{\Gamma}^{j0}}\left(\vec{\xi}_{\mathcal{B}}\right) = \frac{1}{2\,\mu^0}\Bigg[&\frac{\boldsymbol{I}\overline{\otimes}\left[\vec{\beta}^j\left(\vec{\xi}_{\mathcal{B}}\right)\otimes\vec{\beta}^j\left(\vec{\xi}_{\mathcal{B}}\right)\right] + \boldsymbol{I}\underline{\otimes}\left[\vec{\beta}^j\left(\vec{\xi}_{\mathcal{B}}\right)\otimes\vec{\beta}^j\left(\vec{\xi}_{\mathcal{B}}\right)\right] + \left[\vec{\beta}^j\left(\vec{\xi}_{\mathcal{B}}\right)\otimes\vec{\beta}^j\left(\vec{\xi}_{\mathcal{B}}\right)\right]\overline{\otimes}\boldsymbol{I} + \left[\vec{\beta}^j\left(\vec{\xi}_{\mathcal{B}}\right)\otimes\vec{\beta}^j\left(\vec{\xi}_{\mathcal{B}}\right)\right]\underline{\otimes}\boldsymbol{I}}{2\,\|\vec{\beta}^j\left(\vec{\xi}_{\mathcal{B}}\right)\|^2} \\ &- \frac{\vec{\beta}^j\left(\vec{\xi}_{\mathcal{B}}\right)\otimes\vec{\beta}^j\left(\vec{\xi}_{\mathcal{B}}\right)\otimes\vec{\beta}^j\left(\vec{\xi}_{\mathcal{B}}\right)\otimes\vec{\beta}^j\left(\vec{\xi}_{\mathcal{B}}\right)}{\|\vec{\beta}^j\left(\vec{\xi}_{\mathcal{B}}\right)\|^4}\Bigg] \quad \forall\vec{\xi}_{\mathcal{B}} \text{ with } \vec{\beta}^j\left(\vec{\xi}_{\mathcal{B}}\right)\neq\vec{0} \quad . \end{aligned} \tag{41}$$

Restricting ourselves to a two-dimensional setting, it is observed that the Eshelby-Green operator $\widehat{\boldsymbol{\Gamma}^{j0}}\left(\vec{\xi}_{\mathcal{B}}\right)$ is not defined at the frequencies

$$\vec{\xi}_{\mathcal{B}} \in \left\{\vec{0},\, \frac{\pi\,\mathfrak{n}_1^j}{L_1}\,\vec{e}_1,\, \frac{\pi\,\mathfrak{n}_2^j}{L_2}\,\vec{e}_2,\, \frac{\pi\,\mathfrak{n}_1^j}{L_1}\,\vec{e}_1 + \frac{\pi\,\mathfrak{n}_2^j}{L_2}\,\vec{e}_2\right\} \quad , \tag{42}$$

with $\mathfrak{n}_i^j$ denoting the number of grid points at discretisation level j in spatial direction $\vec{\mathrm{e}}_i$, for

$$\vec{\beta}^j\left(\vec{\vec{\xi}}_{\mathcal{B}}\right) = \sum_n \sum_k \frac{c_k}{\eta_n^j} \sin\left(k\,\eta_n^j\,\vec{\vec{\xi}}_{\mathcal{B}} \cdot \vec{\mathrm{e}}_n\right) \vec{\mathrm{e}}_n = \vec{0} \quad , \tag{43}$$

holds. In accordance with the developments on Eshelby-Green operators for finite difference-based discretisations, the classic choices to remedy this problem consist of either enforcing the strains or the stresses (in the converged state) at the critical frequencies $\vec{\vec{\xi}}_{\mathcal{B}}$ (except for the origin) to vanish, see the discussion in, e.g., [34]. The first choice amounts to setting $\widehat{\boldsymbol{\Gamma}^{j0}}\left(\vec{\vec{\xi}}_{\mathcal{B}}\right) = \mathbf{0}$ whereas the second choice can for instance be enforced by setting $\widehat{\boldsymbol{\Gamma}^{j0}}\left(\vec{\vec{\xi}}_{\mathcal{B}}\right) = \left[\mathbf{E}^0\right]^{-1}$ for all critical frequencies except for $\vec{\vec{\xi}}_{\mathcal{B}} = \vec{0}$ which corresponds to the prescribed average strain $\boldsymbol{\varepsilon}_{\mathrm{M}}$.

In contrast to the discussion at the end of Section 3.1 and the Eshelby-Green operator $\widehat{\boldsymbol{\Gamma}^0}\left(\vec{\vec{\xi}}_{\mathcal{B}}\right)$, it is also observed that the Nyquist frequencies (except for those included in (42)) do not require special treatment for the strain fields in (29) to be real-valued. To see this, consider for instance the Nyquist frequency pair

$${}^{*}\vec{\vec{\xi}}^{\,\mathrm{c}}_{\mathcal{B}} = \xi_{\mathcal{B}1}\,\vec{\mathrm{e}}_1 + \xi^{\mathrm{c}}_{\mathcal{B}2}\,\vec{\mathrm{e}}_2 \quad , \quad {}^{\bullet}\vec{\vec{\xi}}^{\,\mathrm{c}}_{\mathcal{B}} = -\xi_{\mathcal{B}1}\,\vec{\mathrm{e}}_1 + \xi^{\mathrm{c}}_{\mathcal{B}2}\,\vec{\mathrm{e}}_2 \quad , \tag{44}$$

indicated by superscripts * and $^{\bullet}$, and observe that

$$\vec{\beta}^j\left({}^{*}\vec{\vec{\xi}}^{\,\mathrm{c}}_{\mathcal{B}}\right) = \sum_k \frac{c_k}{\eta_n^j} \sin\left(k\,\eta_n^j\,\vec{\vec{\xi}}_{\mathcal{B}} \cdot \vec{\mathrm{e}}_1\right) \vec{\mathrm{e}}_1 = -\vec{\beta}^j\left({}^{\bullet}\vec{\vec{\xi}}^{\,\mathrm{c}}_{\mathcal{B}}\right) \quad , \tag{45}$$

holds. With (45) at hand, the evaluation of (41) eventually results in

$$\widehat{\boldsymbol{\Gamma}^{j0}}\left({}^{*}\vec{\vec{\xi}}^{\,\mathrm{c}}_{\mathcal{B}}\right) = \widehat{\boldsymbol{\Gamma}^{j0}}\left({}^{\bullet}\vec{\vec{\xi}}^{\,\mathrm{c}}_{\mathcal{B}}\right) \quad . \tag{46}$$

In particular, it is noted that $\widehat{\boldsymbol{\Gamma}^{j0}}\left({}^{*}\vec{\vec{\xi}}^{\,\mathrm{c}}_{\mathcal{B}}\right)$ and $\widehat{\boldsymbol{\Gamma}^{j0}}\left({}^{\bullet}\vec{\vec{\xi}}^{\,\mathrm{c}}_{\mathcal{B}}\right)$ are real-valued fourth order tensors such that the requirement of $\widehat{\boldsymbol{\Gamma}^{j0}}\left({}^{*}\vec{\vec{\xi}}^{\,\mathrm{c}}_{\mathcal{B}}\right)$ being the complex-conjugate of $\widehat{\boldsymbol{\Gamma}^{j0}}\left({}^{\bullet}\vec{\vec{\xi}}^{\,\mathrm{c}}_{\mathcal{B}}\right)$ is fulfilled.

3.3. Barzilai-Borwein scheme

The Moulinec-Suquet basic scheme is rather slow compared to state of the art solution approaches [21] . In particular, its convergence rate significantly depends on the chosen reference material and the scheme may fail to converge for a poor choice – e.g. for a "too" soft reference material. Against this background, an extended version of the basic scheme that is competitive to the fastest solvers available was proposed in [28]. The scheme relies on the interpretation of the basic scheme as a gradient decent method and makes use of the Barzilai-Borwein step size control [62]. More specifically speaking, the update scheme

$${}^{n+1}\boldsymbol{\varepsilon}\left(\vec{x}\right) = {}^{n}\boldsymbol{\varepsilon}\left(\vec{x}\right) - {}^{n}\gamma\,\boldsymbol{\Gamma}^0\left({}^{n}\boldsymbol{\sigma}\left(\vec{x}\right)\right) \quad , \tag{47}$$

with the recursive update

$${}^{n}\gamma = {}^{n-1}\gamma\left[1 - \frac{\left\langle \boldsymbol{\Gamma}^0\left({}^{n}\boldsymbol{\sigma}\left(\vec{x}\right)\right), \boldsymbol{\Gamma}^0\left({}^{n-1}\boldsymbol{\sigma}\left(\vec{x}\right)\right)\right\rangle_{L^2}}{\left\|\boldsymbol{\Gamma}^0\left({}^{n-1}\boldsymbol{\sigma}\left(\vec{x}\right)\right)\right\|^2_{L^2}}\right]^{-1} \quad , \quad {}^{0}\gamma = 1 \quad , \tag{48}$$

for the Barzilai-Borwein step size γ, motivated by the incorporation of second-order information in gradient decent methods, was proposed. In the light of (31) it is observed that the step size control, in essence, can be interpreted as an adaptive adjustment of the reference material.

3.4. Convergence criterion

In accordance with [28, 21], the convergence criterion

$$E^0 \, \frac{\| \boldsymbol{\Gamma}^0 \left({}^n\sigma \left(x \right) \right) \|_{L^2}}{| \left\langle {}^n\sigma \left(x \right) \right\rangle |} < \epsilon_{\mathrm{F}} \quad , \quad \text{one-dimensional setting} \tag{49a}$$

$$2\,\mu^0 \, \frac{\| \boldsymbol{\Gamma}^0 \left({}^n\boldsymbol{\sigma} \left(\vec{x} \right) \right) \|_{L^2}}{\| \left\langle {}^n\boldsymbol{\sigma} \left(\vec{x} \right) \right\rangle \|_{\mathrm{Fro}}} < \epsilon_{\mathrm{F}} \quad , \quad \text{two-dimensional setting} \tag{49b}$$

is adopted in this contribution with ϵ_{F} denoting a preset convergence tolerance. In virtue of (29) and (47), (49) can be interpreted as a condition on the (normalised) step size in strain space when neglecting the Barzilai-Borwein step size control since

$${}^{n+1}\boldsymbol{\varepsilon} \left(\vec{x} \right) - {}^n\boldsymbol{\varepsilon} \left(\vec{x} \right) = - \, \boldsymbol{\Gamma}^0 \left({}^n\boldsymbol{\sigma} \left(\vec{x} \right) \right) \quad \text{for} \quad {}^n\gamma = 1.0 \quad , \tag{50}$$

holds.

4. Wavelet-enhanced FFT-based spectral solver

The fundamentals of the wavelet-enhanced adaptive hierarchical FFT-based approach proposed in this contribution will be discussed in this section. The underlying key idea is to significantly reduce the number of material model evaluations $\mathrm{n_{mat}}$ by representing the stress field on a hierarchical wavelet basis. In other words, the material model is only evaluated where deemed necessary and a wavelet-based approximation of the stress field is used otherwise. Note that the wavelet-based discretisation naturally entails a refinement criterion: Additional higher-level grid points are only activated (in the sense that the material model is evaluated) in regions where "high" wavelet coefficients are encountered. For the interpolating wavelet family considered in the present contribution, the occurrence of "high" wavelet coefficients implies, in the light of (14), a significant approximation error of the stresses at the corresponding grid point, if the grid point would not be taken into consideration in the wavelet expansion of the stress field, i.e. in relation (8).

By activating only a reduced set of grid points at each discretisation level and by successively progressing to higher discretisation levels, the proposed approach is adaptive and, in particular, exploits the natural hierarchy associated with wavelet discretisations. This is in striking contrast to established non-adaptive FFT-based spectral approaches in which the material model is evaluated at every grid point of the underlying regular structured grid. Detailed information on the proposed procedure in a one-dimensional setting is provided in Section 4.1. The two-dimensional extension is discussed in Section 4.2 and the overall numerical effort of the method is analysed in Section 4.3.

4.1. One-dimensional approach

To calculate a wavelet-based approximation of the stress field in a one-dimensional setting the following steps, as exemplified in Figure 5, are taken:

- **Step 0:** Assume the grid point values of the strain field, $[{}^n\varepsilon]_k^j = {}^n\varepsilon\left(x_k^j\right)$, in iteration n to be given.
- **Step 1:** Evaluate the material model for each grid point at discretisation level 0 and assign the scaling function coefficients of the stress field by using the interpolating property of the wavelet family, i.e. set $[s^\sigma]_k^0 \leftarrow [{}^n\sigma]_k^0$.
- **Step 2:** Define the index set of all grid points at discretisation level 1 where the material model is to be evaluated, i.e. $\mathcal{M}^1 = \left\{ k \in \mathbb{Z} : \text{the grid point at } x_k^1 \text{ occurs for the first time at discretisation level } 1 \right\}$ and set counter $j = 0$.
- **Step 3:** Evaluate the material model to determine the stresses $[{}^n\sigma]_k^{j+1}$ for $k \in \mathcal{M}^{j+1}$.
- **Step 4:** Calculate a level j+1 approximation of the wavelet-discretised stress field by carrying out the backward wavelet transform (12) with $\left[\underline{d}^\sigma\right]^j = \underline{0}$, i.e.

$$\left[\underline{s}^\sigma\right]^{j+1} = \underline{\underline{B}}_j^{j+1} \left[\begin{matrix} \left[\underline{s}^\sigma\right]^j \\ \underline{0} \end{matrix} \right] \quad .$$

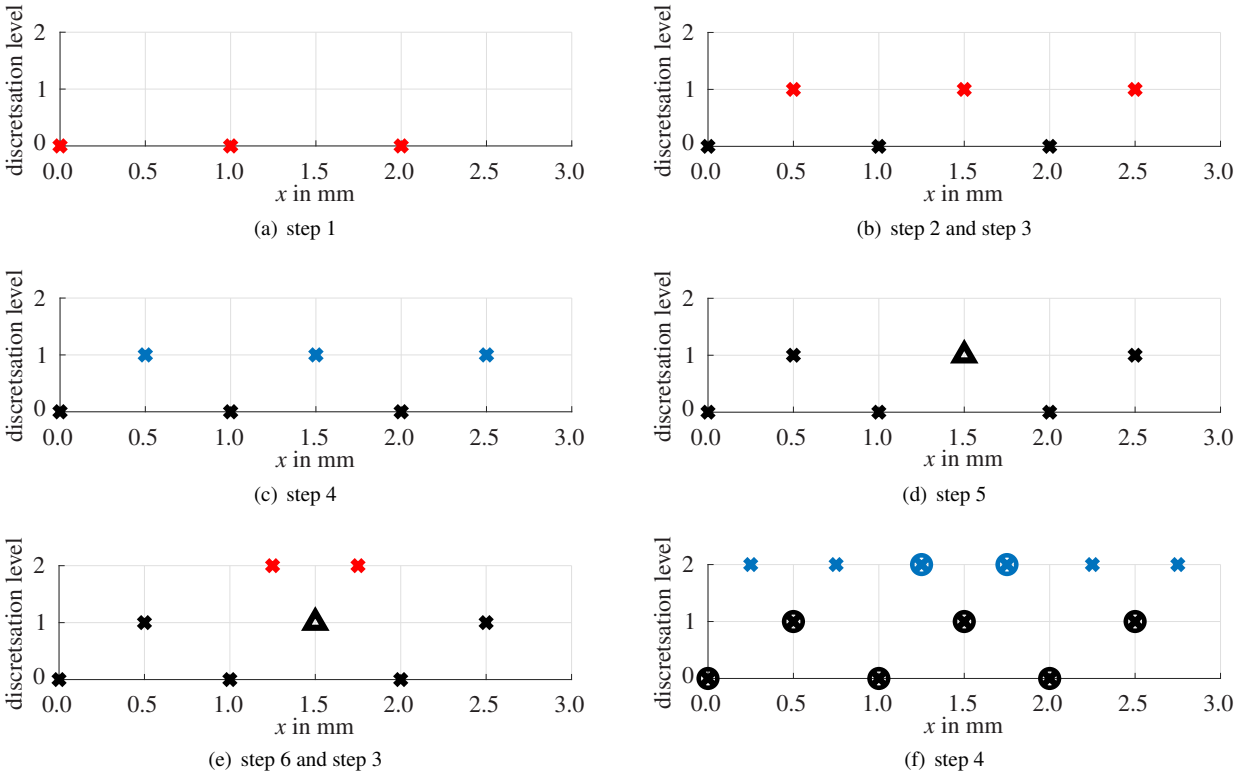

Figure 5: Grid adaptation in a one-dimensional setting. a) Evaluation of material model at level 0 grid points (red-coloured). b) Definition of index set $\mathcal{M}^1$ and evaluation of material model at level 1 grid points (red-coloured). c) Approximation of stress field at level 1 grid points (blue-coloured) through wavelet synthesis. d) Determination of the set of critical grid points C^1 (marked with $\triangle$). e) Definition of index set $\mathcal{M}^2$ and evaluation of material model at level 2 grid points (red-coloured). f) Approximation of stress field at level 2 grid points (blue-coloured) by means of wavelet synthesis. To highlight the reduction in the number of material model evaluations, grid points where the material model was evaluated are additionally encircled.

- **Step 5:** Determine the index set of critical grid points at discretisation level $j+1$ where the relative error in the wavelet-approximated stress field exceeds the tolerance ϵ_W, i.e. $C^{j+1} = \left\{ k \in \mathcal{M}^{j+1} : \frac{\left| [s^\sigma]_k^{j+1} - [{}^n\sigma]_k^{j+1} \right|}{\left| [{}^n\sigma]_k^{j+1} \right|} > \epsilon_W \right\}$.
- **Step 6:** Take neighbouring grid points at the next higher resolution level into account. I.e. activate material model evaluations at level $j+2$ grid points defined by the index set $\mathcal{M}^{j+2} = \left\{ k \in \mathbb{Z} : (k = 2n-1) \vee (k = 2n+1), n \in C^{j+1} \right\}$ when passing from level $j+1$ to level $j+2$.
- **Step 7:** Correct the wavelet approximated level $j+1$ stress values $[s^\sigma]_k^{j+1}$ by making use of the stress values resulting from the material model evaluation $[{}^n\sigma]_k^{j+1}$, i.e. set $[s^\sigma]_k^{j+1} \leftarrow [{}^n\sigma]_k^{j+1}$ for $k \in \mathcal{M}^{j+1}$.
- **Step 8:** *If* level $j+1$ is the maximal discretisation level, use the wavelet-approximated stresses $[s^\sigma]_k^{j+1}$ at the grid points to carry out an FFT update step according to (32). *Else*, increase the level counter $j \leftarrow j+1$ and proceed with Step 3.

4.2. Two-dimensional approach

In analogy to the one-dimensional approach discussed in Section 4.1, the following steps, as exemplified in Figure 6, are taken in a two-dimensional setting to obtain a wavelet-approximation of the stress field:

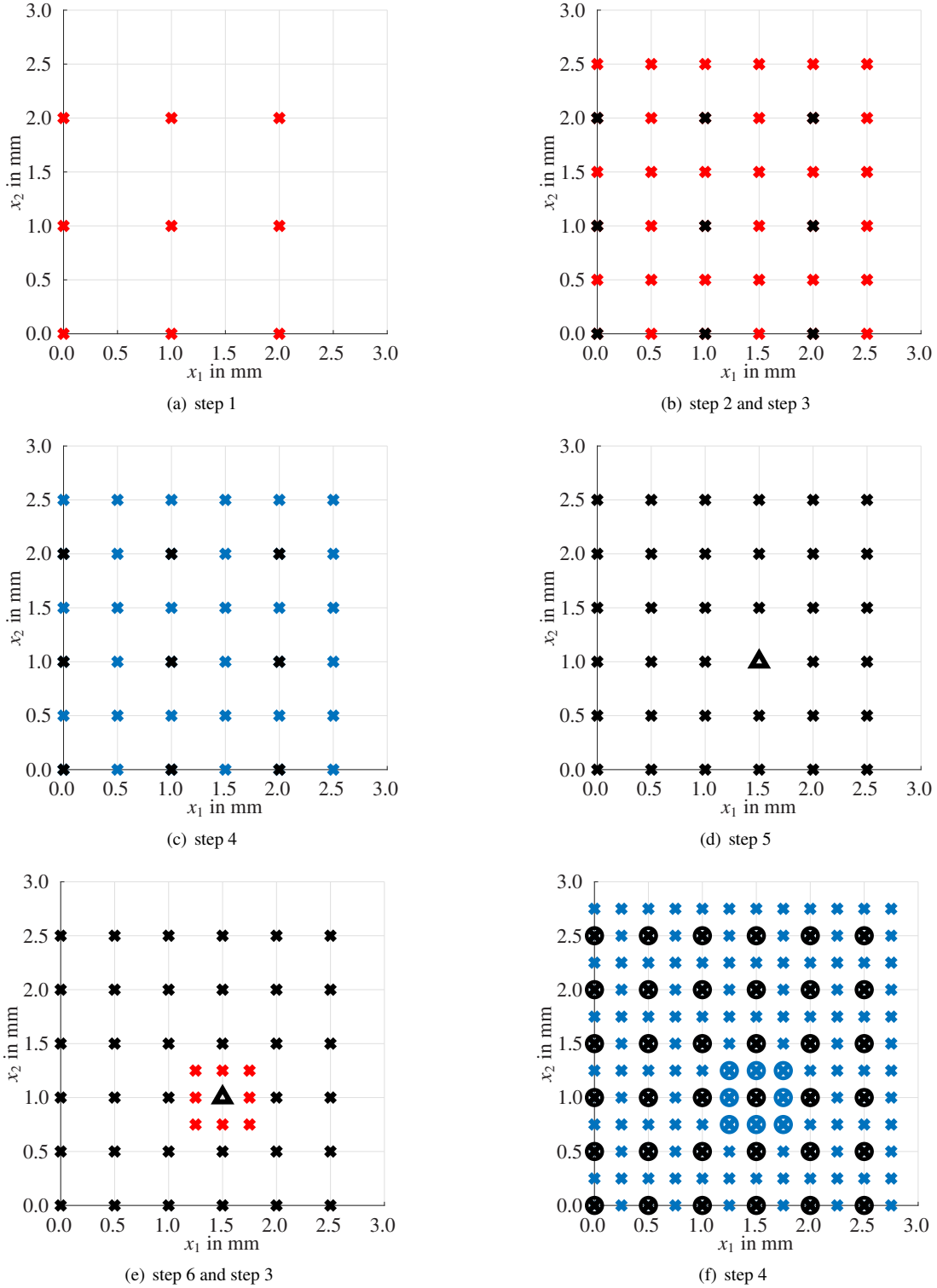

(a) step 1

(b) step 2 and step 3

(c) step 4

(d) step 5

(e) step 6 and step 3

(f) step 4

Figure 6: Grid adaptation in a two-dimensional setting. a) Evaluation of material model at level 0 grid points (red-coloured). b) Definition of index set $\mathcal{M}^1$ and evaluation of material model at level 1 grid points (red-coloured). c) Approximation of stress field at level 1 grid points (blue-coloured) through wavelet synthesis. d) Determination of the set of critical grid points $\mathcal{C}^1$ (marked with $\triangle$). e) Definition of index set $\mathcal{M}^2$ and evaluation of material model at level 2 grid points (red-coloured). f) Approximation of stress field at level 2 grid points (blue-coloured) by means of wavelet synthesis. To highlight the reduction in the number of material model evaluations, grid points where the material model was evaluated are additionally encircled.

- **Step 0:** Assume the grid point values of the strain field, $[{}^n\boldsymbol{\varepsilon}]^j_{k;l} = {}^n\boldsymbol{\varepsilon}\left(\vec{x}^j_{k;l}\right)$, in iteration step n to be given.
- **Step 1:** Evaluate the material model for each grid point at discretisation level 0 and assign the scaling function coefficients of the stress field, ${}^n\boldsymbol{\sigma}(\vec{x}) = {}^n\sigma_{qr}(\vec{x})\,\vec{e}_q \otimes \vec{e}_r$, by using the interpolating property of the wavelet family, i.e. set ${}^0[S^{\sigma_{qr}}]^0_{k;l} \leftarrow \left[{}^n\sigma_{qr}\right]^0_{k;l}$.
- **Step 2:** Define the (multi-)index set of all grid points at discretisation level 1 where the material model is to be evaluated, i.e. $\mathcal{M}^1 = \left\{(k,l) \in \mathbb{Z}^2 : \text{the grid point at } \vec{x}^1_{k;l} \text{ occurs for the first time at discretisation level } 1\right\}$ and set $j = 0$.
- **Step 3:** Evaluate the material model to determine the stress values $[{}^n\boldsymbol{\sigma}]^{j+1}_{k;l}$ for $(k,l) \in \mathcal{M}^{j+1}$.
- **Step 4:** Calculate a level j+1 approximation of the wavelet-discretised stress field by coefficient-wise carrying out the backward wavelet transform (22) with ${}^p\left[\underline{\underline{S}}^{\sigma_{qr}}\right]^0 = \underline{\underline{0}}$, $p \in \{1,2,3\}$, i.e.

$${}^0\left[\underline{\underline{S}}^{\sigma_{qr}}\right]^{j+1} = \underline{\underline{B}}^{j+1}_j \begin{bmatrix} {}^0\left[\underline{\underline{S}}^{\sigma_{qr}}\right]^j & \underline{\underline{0}} \\ \underline{\underline{0}} & \underline{\underline{0}} \end{bmatrix} \left[\underline{\underline{B}}^{j+1}_j\right]^{\mathrm{t}} \quad .$$

- **Step 5:** Determine the index set of critical grid points at discretisation level $j+1$ where the relative error in the wavelet-approximated stress field exceeds the tolerance ϵ_{W}, i.e. $C^{j+1} = \left\{(k,l) \in \mathcal{M}^{j+1} : \frac{\left\|\left[\sum_q \sum_r {}^0[S^{\sigma_{qr}}]^{j+1}_{k;l}\,\vec{e}_q \otimes \vec{e}_r\right] - [{}^n\boldsymbol{\sigma}]^{j+1}_{k;l}\right\|_{\mathrm{Fro}}}{\left\|[{}^n\boldsymbol{\sigma}]^{j+1}_{k;l}\right\|_{\mathrm{Fro}}} > \epsilon_{\mathrm{W}}\right\}$.
- **Step 6:** Take neighbouring grid points at the next higher resolution level into account. I.e. activate material model evaluations at level j+2 grid points defined by the (multi-)index set $\mathcal{M}^{j+2} = \Big\{(k,l) \in \mathbb{Z}^2 : (2n-1, 2m-1) \vee (2n-1, 2m) \vee (2n-1, 2m+1) \vee (2n, 2m-1) \vee (2n, 2m+1) \vee (2n+1, 2m-1) \vee (2n+1, 2m) \vee (2n+1, 2m+1), (n,m) \in C^{j+1}\Big\}$ when passing from level $j+1$ to level $j+2$.
- **Step 7:** Correct the wavelet approximated level $j+1$ stress values ${}^0[S^{\sigma_{qr}}]^{j+1}_{k;l}$ by making use of the stresses resulting from the material model evaluation $[{}^n\boldsymbol{\sigma}]^{j+1}_{k;l}$, i.e. set ${}^0[S^{\sigma_{qr}}]^{j+1}_{k;l} \leftarrow \left[{}^n\sigma_{qr}\right]^{j+1}_{k;l}$ for $(k,l) \in \mathcal{M}^{j+1}$.
- **Step 8:** *If* level $j+1$ is the maximal discretisation level, use the wavelet-approximated stresses $\sum_q \sum_r {}^0[S^{\sigma_{qr}}]^{j+1}_{k;l}\,\vec{e}_q \otimes \vec{e}_r$ at the grid points to carry out an FFT update step according to (29). *Else*, increase the level counter $j \leftarrow j+1$ and proceed with Step 3.

4.3. Additional numerical effort associated with the wavelet transforms

The wavelet-based approximation of the stress field in Step 4 of the algorithms discussed in Section 4.1 and Section 4.2 is associated with additional floating point operations. To increase the overall efficiency of the numerical scheme, the numerical effort associated with the backward wavelet transforms needs to be (significantly) smaller than the one associated with the evaluation of the material model. Sophisticated material models that are for instance used to simulate plastic deformation processes and that, in general, require the numerical solution of a non-linear system of ordinary differential equations are computationally very demanding. In comparison, the numerical effort associated with the wavelet transform is expected to be almost negligible as will be shown in this section.

In virtue of (11) and for the particular interpolating wavelet family chosen, it is observed that the wavelet transform to approximate the stress state at even grid points x^j_{2k}, (13), is the identity map. At odd grid points and for $[d^\sigma]^j_k = 0$ (as assumed in Step 4), relation (14) reduces to

$$[s^\sigma]^{j+1}_{2k+1} = -\frac{1}{16}\,[s^\sigma]^j_{k+2} + \frac{9}{16}\,[s^\sigma]^j_{k+1} + \frac{9}{16}\,[s^\sigma]^j_k - \frac{1}{16}\,[s^\sigma]^j_{k-1} \tag{51}$$

such that (without factorisation) $\#Add = 3$ additions and $\#Mul = 4$ multiplications are required to calculate the wavelet-based stress approximation at a particular grid point in Step 4.

Accordingly, the overall numerical effort $\mathrm{e}_{1\mathrm{D}}$ when considering a discretisation with $\mathfrak{n}_1^0$ grid points on level 0 and $\mathfrak{n}_1^{\mathrm{n}_\mathcal{G}} = 2^{\mathrm{n}_\mathcal{G}}\,\mathfrak{n}_1^0$ grid points at the highest discretisation level $\mathrm{n}_\mathcal{G}$, reads

$$\mathrm{e}_{1\mathrm{D}} = \sum_{j=0}^{\mathrm{n}_\mathcal{G}-1} 2^j\,\mathfrak{n}_1^0\;[\#Add + \#Mul] = \left[\mathfrak{n}_1^{\mathrm{n}_\mathcal{G}} - \mathfrak{n}_1^0\right][\#Add + \#Mul] \quad . \tag{52}$$

Due to the underlying tensor-product structure adopted in a two-dimensional setting, the two-dimensional wavelet transform in Step 4 reduces to two sequential one-dimensional transformations. Furthermore, by taking into account $\left[\underline{\underline{S}}^{\sigma_{qr}}\right]^0 = \underline{\underline{0}}, p \in \{1,2,3\}$ (as assumed in Step 4) close inspection reveals that $\mathfrak{n}_2^0$ 1D-transformations are required in the first transformation step, whereas $2\,\mathfrak{n}_1^0$ 1D-transformations are required in the second transformation step for a level 0 discretisation with $\mathfrak{n}_1^0 \times \mathfrak{n}_2^0$ grid points. Accordingly, the numerical effort $\mathrm{e}_{2\mathrm{D}}$ when approximating a scalar-valued field and taking $\mathrm{n}_\mathcal{G}$ additional grid levels into account is given by

$$\mathrm{e}_{2\mathrm{D}} = \sum_{j=0}^{\mathrm{n}_\mathcal{G}-1} 3\,\left[2^l\,\mathfrak{n}_1^0\right]\left[2^l\,\mathfrak{n}_2^0\right][\#Add + \#Mul] = \left[\mathfrak{n}_1^{\mathrm{n}_\mathcal{G}}\,\mathfrak{n}_2^{\mathrm{n}_\mathcal{G}} - \mathfrak{n}_1^0\,\mathfrak{n}_2^0\right][\#Add + \#Mul] \tag{53}$$

Since each coefficient of the (symmetric) Cauchy stress tensor is to be approximated, the overall effort for the stress approximation in a two-dimensional setting is $3\left[\mathfrak{n}_1^{\mathrm{n}_\mathcal{G}}\,\mathfrak{n}_2^{\mathrm{n}_\mathcal{G}} - \mathfrak{n}_1^0\,\mathfrak{n}_2^0\right][\#Add + \#Mul]$.

To put the computational effort associated with the wavelet approximation into perspective, consider isotropic linear elasticity, as the most simplistic material model, as a first example. In plane strain or plane stress settings, the linear relation between the stresses and strains can be expressed in an appropriate matrix notation resulting in $\#Add_{\mathrm{el}} = 2$ and $\#Mul_{\mathrm{el}} = 5$ per sampling point. This number is only slightly lower than the $3\,\#Add = 9$ additions and $3\,\#Mul = 12$ multiplications required per grid point for the wavelet transform. Next, consider von Mises-type elasto-plasticity with linear isotropic and kinematic hardening, cf. [63, Chapter 3.3]. The specific structure of the material model allows for a closed-form solution (return-mapping) such that no iterations at material point level are required. However, even in such an idealised setting, a predictor-corrector step needs to be carried out, the state variables need to be updated and the stress state needs to be determined. In a typical implementation this results into $\#Add_{\mathrm{pi}} \approx 60$ and $\#Mul_{\mathrm{pi}} \approx 75$ for isotropic hardening, and $\#Add_{\mathrm{pk}} \approx 80$ and $\#Mul_{\mathrm{pk}} \approx 110$ for combined isotropic and kinematic hardening. Finally, consider a non-linear system of evolution equations featuring multiple (in general tensor-valued) internal variables that is solved by means of an implicit integration scheme. Due to the underlying non-linearity of the problem, several iterations are usually required in the iterative scheme at material point level, which significantly increases the computational effort further as compared to the three elementary examples discussed before.

The previous examples clearly demonstrate that the computational effort associated with the material model evaluation significantly increases with increasing complexity of the constitutive response under consideration and can certainly be expected to be significantly higher than the computational effort associated with the wavelet transform.

5. Representative simulation results

This section focuses on a study of representative boundary value problems that reveal the main properties of the proposed wavelet-enhanced FFT-based solution approach. To this end, one-dimensional unit cells featuring material interfaces and material interphases, respectively, are first considered in Section 5.1. Section 5.2 focuses on the two-dimensional setting and on the influence of the particular structure of the Eshelby-Green operator.

5.1. One-dimensional setting

To gain a basic understanding of the wavelet-enhanced FFT-based spectral approach when applied to continuum mechanics problems, typical one-dimensional boundary value problems for which analytical solutions can be derived are studied in this section. In particular, material interfaces as a prototype for problems that feature weak discontinuities (i.e. jumps in the strain field) are considered first in Section 5.1.1. In a second step, the discontinuities are relaxed by resolving the material interfaces as material interphases of finite thickness, which, however, still results

in significant local changes in the strain field, see Section 5.1.2. For both one-dimensional sample boundary value problems considered, the simple elastic constitutive relation accordingly takes the form

$$\sigma(x) = \widetilde{E}(x)\, \varepsilon(x) \quad , \tag{54}$$

with Young's modulus $\widetilde{E}(x)$ being a function of space as specified in the respective sections.

The periodic one-dimensional domain of length $l = 1\,\text{mm}$ is discretised with $\mathfrak{n}_1^0 = 8$ grid points at discretisation level 0 and a maximum number of $\mathfrak{n}_{\mathcal{G}} = 6$ additional discretisation levels it taken into account, see Figure 7. The average macroscale strain $\varepsilon_{\text{M}} = 0.005$ is applied in a single load step, the stiffness constant of the reference material is set to $E^0 = 0.8\,E$, and the convergence tolerance of the FFT-scheme is set to $\epsilon_{\text{F}} = 10^{-8}$.

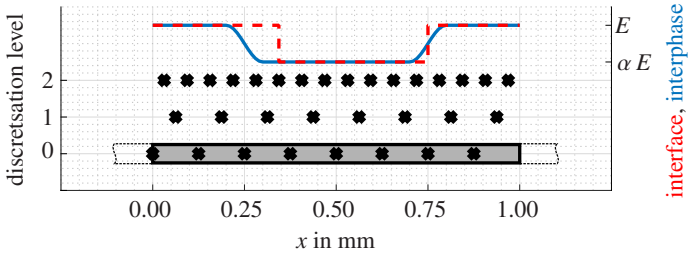

Figure 7: One-dimensional periodic boundary value problem. The first three levels of the nested dyadic grid for a discretion with $\mathfrak{n}_1^0 = 8$ grid points at discretisation level 0 are shown. In addition, the Young's modulus as a function of space for the interface and interphase problem as specified in Section 5.1.1 and Section 5.1.2, respectively, is depicted.

Remark 1 (Wavelet-discretisation in a one-dimensional setting). In a one-dimensional setting, it is observed that the Eshelby-Green operator associated with the Moulinec-Suquet discretisation is constant in Fourier space except for the origin and reduces to the inverse Young's modulus of the reference material, i.e. $\widehat{\Gamma^0}(\xi_{\mathcal{B}}) = \left[E^0\right]^{-1} \forall \xi_{\mathcal{B}} \neq 0$. Moreover, the Nyquist frequencies do not require special treatment for $\widehat{\Gamma^0}(\xi_{\mathcal{B}})$ being constant.

In contrast, focusing on the wavelet-based discretisation, it is observed that the Eshelby-Green operator is constant except for the critical frequencies (which correspond to the origin and the Nyquist frequencies in a one-dimensional setting), where it is not well-defined. In addition, the structure of the Eshelby-Green operator for wavelet-based discretisations reveals striking similarities with the one for finite difference schemes, cf. Section 3.2. For the one-dimensional setting, the particular choice $\widehat{\Gamma^{j0}}\left(\frac{\pi \mathfrak{n}^j}{L}\right) = \frac{1}{E^0}$ will be adopted in the following such that the Eshelby-Green operator associated with the wavelet discretisation and the one associated with the Moulinec-Suquet discretisation are identical. The alternative choice, $\widehat{\Gamma^{j0}}\left(\frac{\pi \mathfrak{n}^j}{L}\right) = 0$, is briefly discussed in Appendix B.

5.1.1. Material interfaces

This section focuses on the principal properties of the proposed formulation in the presence of weak discontinuities, i.e. jumps in the strain field. Classical FFT-based solution techniques rely on a regular grid in physical space which significantly increases the computational effort when strongly localised changes in the solution profile occur. In essence, the smallest features in the solution domain that are to be resolved govern the (constant) grid spacing and hence the number of material model evaluations. Note that material interfaces may not necessarily be positioned at grid points but may occur at arbitrary places in the solution domain – either due to changes in the underlying microstructure or, for instance, due to the evolution of elasto-plastic transition zones. Properly resolving the position and evolution of (possibly multiple) weak discontinuities thus requires a fine discretisation which is, however, not necessary in most parts of the solution domain. In striking contrast to classical FFT-based approaches, it will be shown in this section that by using the proposed wavelet-enhanced FFT approach, a targeted refinement is possible and that higher-level grid points are only activated in the vicinity of the discontinuities.

To this end, a truss-like structure that consists of two materials with significantly different properties as sketched in Figure 7 is considered. Without loss of generality, the positions of the material interfaces ($x_1 = \frac{11}{32}\text{mm}$, $x_2 = 0.75\,\text{mm}$) are chosen such that they coincide with level 2 and level 0 grid points, respectively. In particular, note that assuming

the material interfaces to be positioned at $\tilde{x}_1 = x_1 - c\,\eta^{\mathrm{n_G}}$ and $\tilde{x}_2 = x_2 - c\,\eta^{\mathrm{n_G}}$ with $c \in [0, 1)$, i.e. in between two neighbouring grid points at the highest discretisation level, would not affect the solution scheme but only the accuracy of the solution. Accordingly, the spatial distribution of the Young's modulus takes the form

$$\widetilde{E}(x) = \begin{cases} E, & \text{if} \quad 0 \le x < x_1 \\ \alpha\, E, & \text{if} \quad x_1 \le x < x_2 \\ E, & \text{if} \quad x_2 \le x < l \end{cases} \quad , \tag{55}$$

with material constants $E = 210\,\mathrm{GPa}$ and $\alpha = 0.6$. By following standard procedure, the closed-form solution for the constant stress field $\sigma(x) = \sigma_{\mathrm{M}}$ as a function of the the applied macroscale strain ε_{M} takes the form

$$\Delta l = \sum_{i=1}^{3} \Delta l_i = \left[\frac{x_1}{E} + \frac{x_2 - x_1}{\alpha E} + \frac{l - x_2}{E} \right] \sigma_{\mathrm{M}} = l\, \varepsilon_{\mathrm{M}} \quad . \tag{56}$$

Moreover, with (55) and (56) at hand, and by inverting (54) a closed-form solution for the (non-constant) microscale strain field $\varepsilon(x)$ can be derived.

The convergence rate of the fixed-point scheme with Barzilai-Borwein step size control is shown as a function of refinement tolerance ϵ_{W} in Figure 8(a). It is observed that the convergence rate for the non-adaptive reference calculation and for moderate refinement tolerances is almost the same. For high values of the refinement tolerance (e.g. $\epsilon_{\mathrm{W}} = 10^{-2}$) that correspond to rather inaccurate approximations of the stress field, a higher number of iterations is required which can be explained by the inaccuracies induced by the stress approximation.

Taking a closer look at the overall number of material model evaluations and the accuracy of the macroscale stresses shown in Figure 8(b), a significant drop in the number of material model evaluations from 1536 to 168 (for $\epsilon_{\mathrm{W}} = 10^{-4}$ and $\epsilon_{\mathrm{W}} = 10^{-3}$) and to 160 (for $\epsilon_{\mathrm{W}} = 10^{-2}$) is observed. The reduction in the accuracy of the macroscale stresses when compared with the analytical solution is negligible for the refinement tolerances $\epsilon_{\mathrm{W}} = 10^{-4}$ and $\epsilon_{\mathrm{W}} = 10^{-3}$, and even acceptable for a refinement tolerance $\epsilon_{\mathrm{W}} = 10^{-2}$.

The previous observations suggest that the proposed formulation permits to maintain (almost) the same level of accuracy while significantly reducing the number of material model evaluations. In this regard, the adaptive selection of critical grid points at which the material model is to be evaluated is key. This is shown in Figure 9 which visualises the set of active grid points for each iteration and various refinement tolerances. Clearly, grid points up to the highest discretisation level are only activated in the vicinity of the material interfaces to accurately capture the stress profile in the first few iterations. Moreover, only level 0 and level 1 grid points are activated in the last three iterations for $\epsilon_{\mathrm{W}} = 10^{-2}$ and in the last iteration for $\epsilon_{\mathrm{W}} = 10^{-3}$ and $\epsilon_{\mathrm{W}} = 10^{-4}$, respectively. This observation can be explained by the fact that the stress distribution in the converged state is constant (within numerical tolerances) such that it can

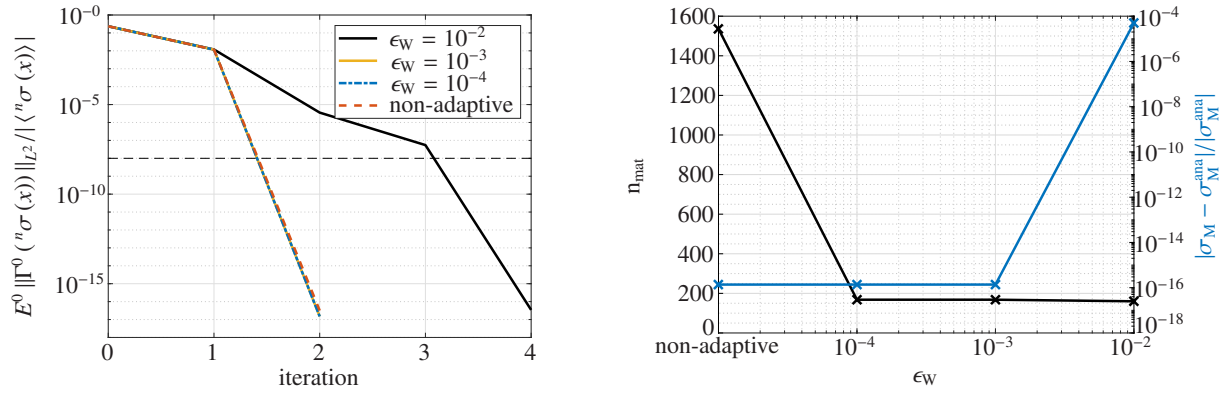

(a) convergence history

(b) material model evaluations and macroscale stress

Figure 8: Convergence history, number of material model evaluations and error in macroscale stresses as a function of refinement tolerance ϵ_{W} for the material interface problem shown in Figure 7. The convergence tolerance $\epsilon_{\mathrm{F}} = 10^{-8}$ is indicated by the horizontal dashed line in a).

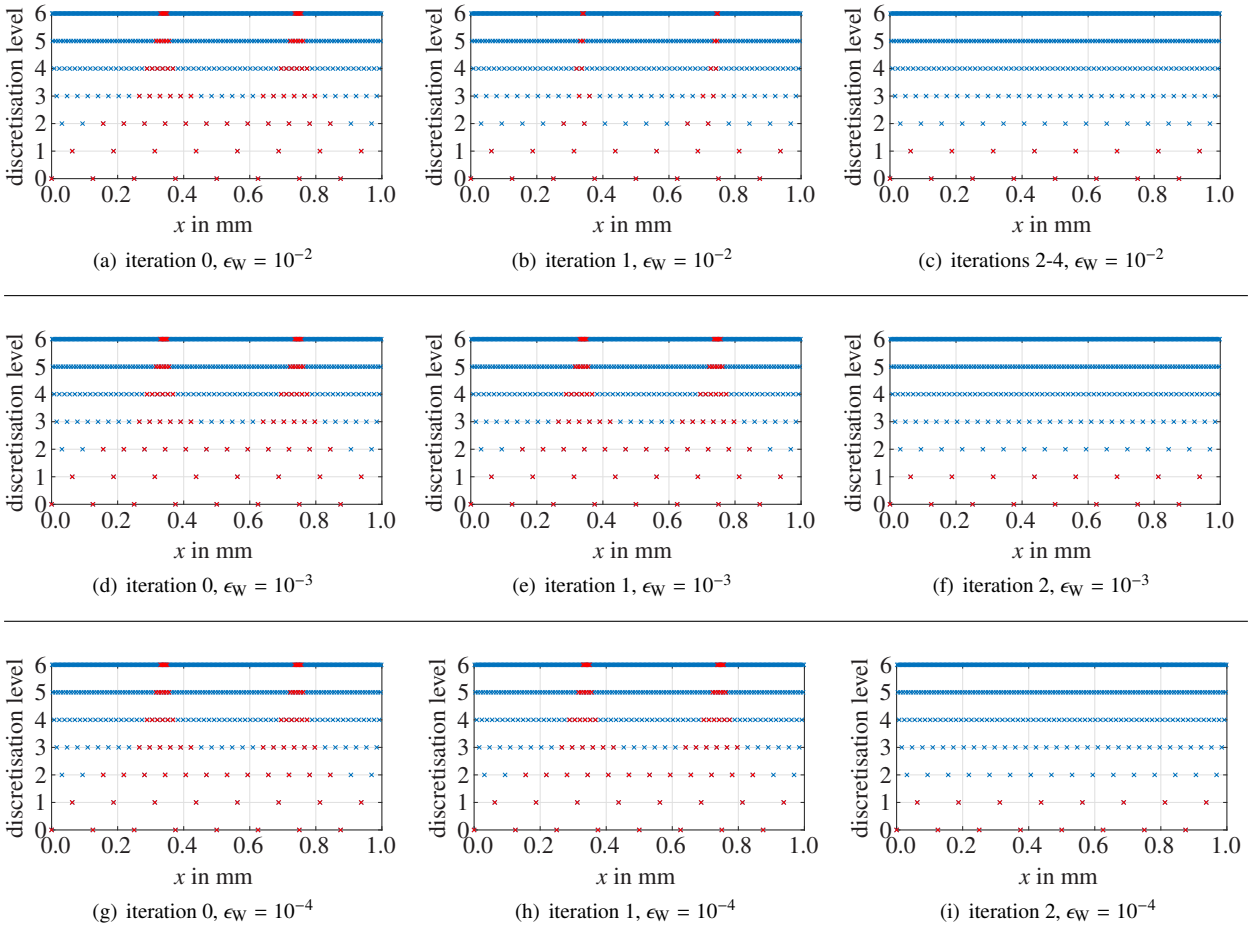

(a) iteration 0, $\epsilon_W = 10^{-2}$ (b) iteration 1, $\epsilon_W = 10^{-2}$ (c) iterations 2-4, $\epsilon_W = 10^{-2}$

(d) iteration 0, $\epsilon_W = 10^{-3}$ (e) iteration 1, $\epsilon_W = 10^{-3}$ (f) iteration 2, $\epsilon_W = 10^{-3}$

(g) iteration 0, $\epsilon_W = 10^{-4}$ (h) iteration 1, $\epsilon_W = 10^{-4}$ (i) iteration 2, $\epsilon_W = 10^{-4}$

Figure 9: Active grid points (red) and inactive grid points (blue) for different iteration steps and various refinement tolerances ϵ_W.

exactly be reproduced by a level 0 wavelet discretisation. Accordingly, no further refinement is triggered in Step 5 of the algorithm proposed in Section 4.1.

Finally, it is remarked that for this particular boundary value problem the refinement tolerances $\epsilon_W = 10^{-4}$ and $\epsilon_W = 10^{-3}$ result in the same activation of grid points.

5.1.2. Material interphases

As a sample problem for localised changes in the solution profile, this section focuses on material interphases. In contrast to the interface problem discussed in Section 5.1.1, the material properties are assumed to change over a region that is finite but significantly smaller than the geometric problem dimensions. The corresponding one-dimensional boundary value problem is sketched in Figure 7. Two different materials and their interphases are defined by the geometrical parameters $x_1 = 0.2\,\mathrm{mm}$, $x_2 = 0.3\,\mathrm{mm}$, $x_3 = 0.7\,\mathrm{mm}$, $x_4 = 0.8\,\mathrm{mm}$, and the spatial distribution of the Young's modulus

$$\widetilde{E}(x) = \begin{cases} E, & \text{if} \quad 0 \le x < x_1 \\ \frac{\alpha+1}{2}\,E + \frac{\alpha-1}{2}\,\cos\left(\left[\frac{x-x_1}{x_2-x_1} - 1\right]\pi\right) E, & \text{if} \quad x_1 \le x < x_2 \\ \alpha\,E, & \text{if} \quad x_2 \le x < x_3 \\ \frac{\alpha+1}{2}\,E + \frac{1-\alpha}{2}\,\cos\left(\left[\frac{x-x_3}{x_4-x_3} - 1\right]\pi\right) E, & \text{if} \quad x_3 \le x < x_4 \\ E, & \text{if} \quad x_4 \le x < l \end{cases} \tag{57}$$

with material parameters $E = 210\,\mathrm{GPa}$ and $\alpha = 0.6$. Following the same procedure as in Section 5.1.1, the closed-form analytical solution for the constant stress field $\sigma(x) = \sigma_\mathrm{M}$ as a function of the applied macroscale strain ε_M reads

$$\Delta l = \sum_{i=1}^{3} \Delta l_i = \left[\frac{x_1}{E} + \frac{x_2 - x_1}{\sqrt{\alpha} E} + \frac{x_3 - x_2}{\alpha E} + \frac{x_4 - x_3}{\sqrt{\alpha} E} + \frac{l - x_4}{E} \right] \sigma_\mathrm{M} = l\, \varepsilon_\mathrm{M} \quad . \tag{58}$$

Likewise, an analytical solution for the microscale strain field follows from inverting (54) and by inserting (57) and (58) into the ensuing equation.

Focusing on the convergence rate as a function of refinement tolerance ϵ_W, it is observed in Figure 10(a) that less iterations are required in the adaptive schemes compared to the non-adaptive one. In particular, the simulation with $\epsilon_\mathrm{W} = 10^{-3}$ requires the least number of iterations. This observation might be attributed to the smoothing effect of the projection of the stress field onto the wavelet basis in conjunction with the one-dimensional character of the problem – i.e. the stress field in the converged state is constant. However, in view of the latter observations and the results for high values of the refinement tolerance discussed in Section 5.1.1, making a general statement on the influence of the wavelet-approximation on the convergence rate of the Barzilai-Borwein-stabilised fixed-point iteration seems not trivially possible.

The overall number of material model evaluations and the accuracy of the predicted macroscale stresses is shown in Figure 10(b) as a function of the refinement tolerance ϵ_W. A significant reduction in the number of material model evaluations with increasing values of the refinement tolerance is observed – reducing 5632 material model evaluations as required in the non-adaptive scheme to 264 in the adaptive scheme with $\epsilon_\mathrm{W} = 10^{-3}$. Regarding the accuracy of the macroscale stresses, an opposite (logical) trend is noticeable – the relative error with respect to the analytical solution increases from $1.59 * 10^{-8}$ for the non-adaptive scheme to $9.49 * 10^{-5}$ for the adaptive scheme with $\epsilon_\mathrm{W} = 10^{-3}$.

Finally, the set of active grid points at each iteration step for various values of the refinement tolerance is shown in Figure 11. In accordance with the findings of Section 5.1.1, higher-level grid points are only activated in the vicinity of the material interphases, i.e. in regions where significant changes in the solution profile are expected. Likewise, only grid points up to level 1 are activated in the last few iterations. Focusing in more detail on the activation of grid points it is observed that grid points up to level 5 are activated but that no grid points at the highest allowed discretisation level are activated for $\epsilon_\mathrm{W} = 10^{-3}$. This is a striking contrast to the interface problem where grid points up to the highest discretisation level were activated for all values of the refinement tolerance analysed (even for $\epsilon_\mathrm{W} = 10^{-1}$ for which the results were not shown). By comparing the activation of grid points for the various refinement tolerances it is moreover observed that 1) higher-level grid points get activated and that 2) more grid points at lower discretisation levels are taken into account for decreasing (tighter) values of the refinement tolerance.

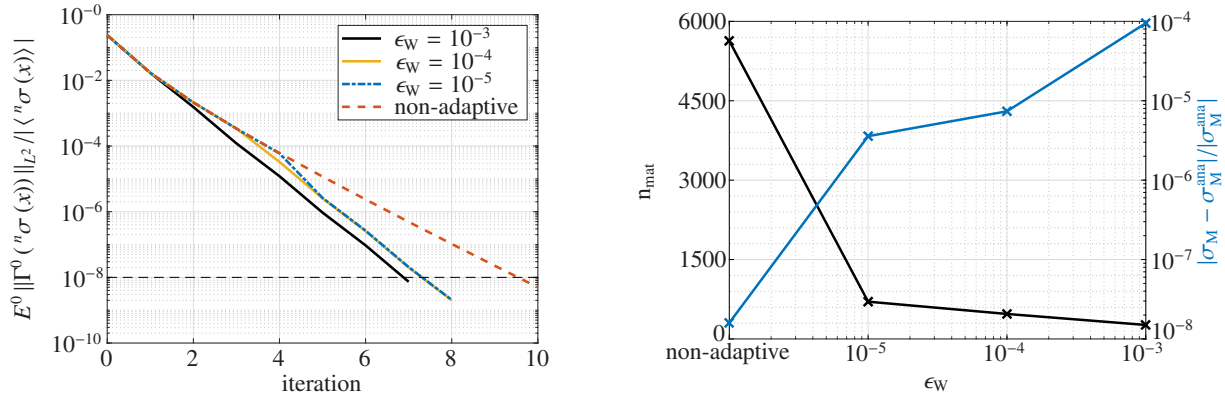

(a) convergence history

(b) material model evaluations and macroscale stress

Figure 10: Convergence history, number of material model evaluations and error in macroscale stresses as a function of refinement tolerance ϵ_W for the material interphase problem sketched in Figure 7. The convergence tolerance $\epsilon_\mathrm{F} = 10^{-8}$ is indicated by a dashed line in a).

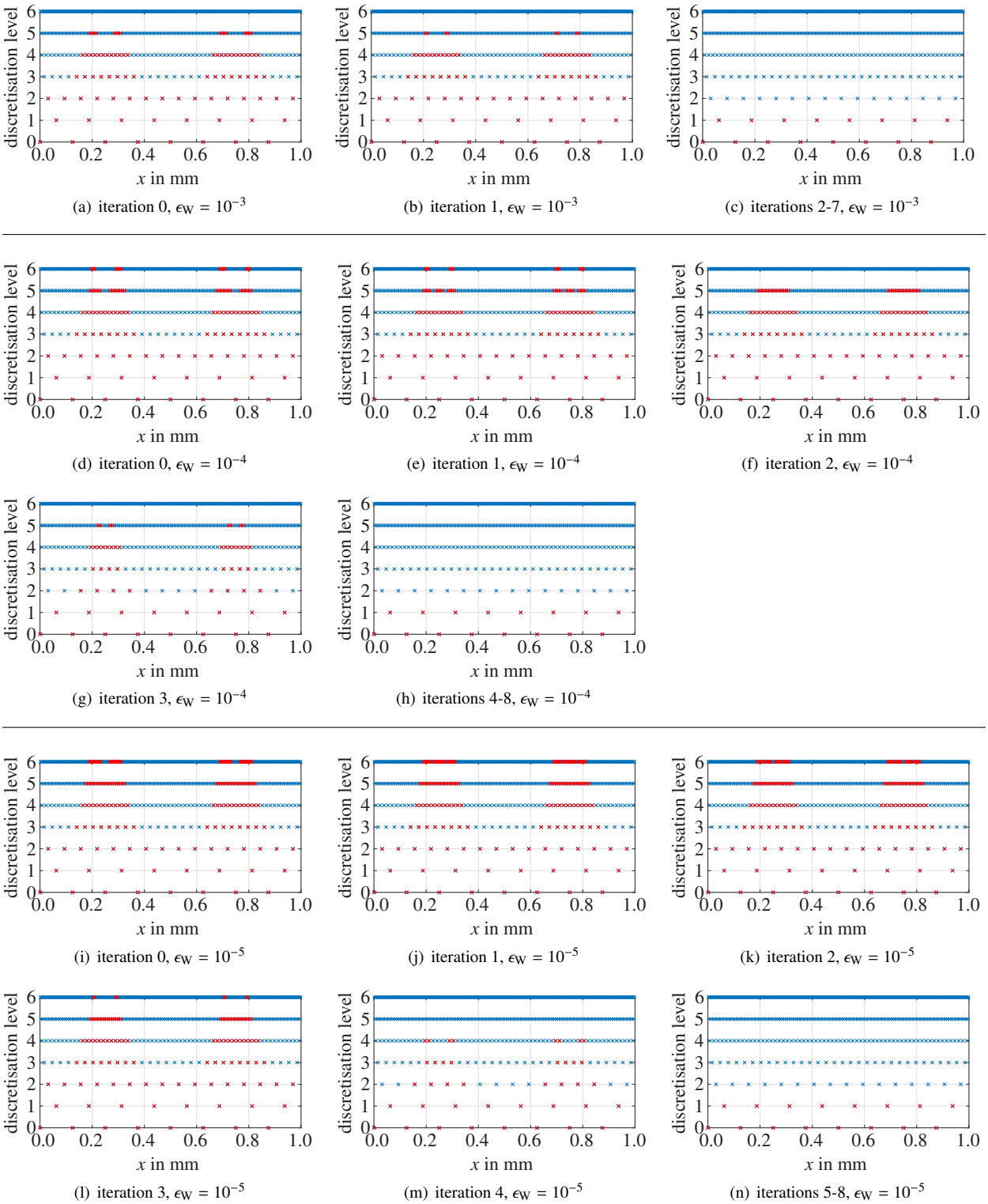

(a) iteration 0, $\epsilon_W = 10^{-3}$ (b) iteration 1, $\epsilon_W = 10^{-3}$ (c) iterations 2-7, $\epsilon_W = 10^{-3}$

(d) iteration 0, $\epsilon_W = 10^{-4}$ (e) iteration 1, $\epsilon_W = 10^{-4}$ (f) iteration 2, $\epsilon_W = 10^{-4}$

(g) iteration 3, $\epsilon_W = 10^{-4}$ (h) iterations 4-8, $\epsilon_W = 10^{-4}$

(i) iteration 0, $\epsilon_W = 10^{-5}$ (j) iteration 1, $\epsilon_W = 10^{-5}$ (k) iteration 2, $\epsilon_W = 10^{-5}$

(l) iteration 3, $\epsilon_W = 10^{-5}$ (m) iteration 4, $\epsilon_W = 10^{-5}$ (n) iterations 5-8, $\epsilon_W = 10^{-5}$

Figure 11: Active grid points (red) and inactive grid points (blue) for different iteration steps and various refinement tolerances ϵ_W.

5.2. Two-dimensional setting

This section focuses on the extension of the one-dimensional studies of Section 5.1 to a two-dimensional setting. To this end, a rectangular unit cell with a circular inclusion as schematically depicted in Figure 12 is considered. For conceptual simplicity, both phases are assumed to show a linear elastic material response

$$\boldsymbol{\sigma} = \mathsf{E} : \boldsymbol{\varepsilon} \quad , \quad \mathsf{E} = \frac{E\,\nu}{[1+\nu]\,[1-2\,\nu]}\,\boldsymbol{I}\otimes\boldsymbol{I} + \frac{E}{2\,[1+\nu]}\left[\boldsymbol{I}\overline{\otimes}\boldsymbol{I} + \boldsymbol{I}\underline{\otimes}\boldsymbol{I}\right] \tag{59}$$

that is governed by the fourth order elasticity tensor E with Young's modulus E and Poisson's ratio ν. The specific material parameters for each phase and the geometric dimensions are summarised in Table 2. The unit cell is subjected to an average (macroscale) tensile strain

$$\boldsymbol{\varepsilon}_{\mathrm{M}} = 0.005\,\vec{e}_1 \otimes \vec{e}_1 \tag{60}$$

in a single load step and plane strain loading conditions are assumed. Moreover, a level 0 discretisation with $\mathrm{n}_1^0 \times \mathrm{n}_2^0 = 8 \times 8$ grid points is considered and a maximum number of $\mathrm{n}_{\mathcal{G}} = 5$ additional discretisation levels is taken into account in the hierarchical wavelet approximation. The reference material in the FFT-based fixed-point iteration is chosen to be of the form (30) with

$$\mu^0 = \frac{E_1}{2\,[1+\nu_1]} \quad , \tag{61}$$

and the Barzilai-Borwein step size control according to Section 3.3 is used for stabilisation purposes. The convergence tolerance (49) is set to $\epsilon_{\mathrm{F}} = 10^{-3}$.

In the following, the focus firstly lies on the influence of the hierarchical wavelet approximation of the stress field on the computational efficiency in terms of material model evaluations and accuracy. To this end, adaptive and non-adaptive simulations based on the classic Eshelby-Green operator associated with a Moulinec-Suquet discretisation are studied in Section 5.2.1. In a second step, calculations based on the Eshelby-Green operator derived in Section 3.2 that takes the underlying wavelet discretisation of the field variables into account are additionally considered in Section 5.2.2.

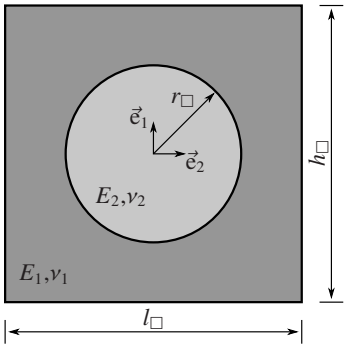

Figure 12: Matrix with soft inclusion.

matrix			
E_1	210 GPa	$l_\square$	1.0 mm
ν_1	0.3	$h_\square$	1.0 mm
inclusion			
E_2	126 GPa	$r_\square$	0.3 mm
ν_2	0.3		

Table 2: Material parameters and geometric dimensions.

5.2.1. Computational efficiency and accuracy

This section focuses on the gain in computational efficiency when enhancing a classic FFT-based multiscale solution approach with an adaptive wavelet scheme. A Moulinec-Suquet discretisation with its associated Eshelby-Green operator (with $\widehat{\boldsymbol{\Gamma}^0}\left(\xi_{\mathcal{B}1}, \xi^{\mathrm{c}}_{\mathcal{B}2}\right) = \widehat{\boldsymbol{\Gamma}^0}\left(\xi^{\mathrm{c}}_{\mathcal{B}1}, \xi_{\mathcal{B}2}\right) = \left[\mathsf{E}^0\right]^{-1}$) is here considered and enhanced by making use of the adaptive hierarchical wavelet approach proposed in Section 4.2. In addition, a high-fidelity finite element calculation, as used in FE^2-based approaches, that relies on a geometrically conforming discretisation of the boundary value problem with 64980 4-node quadrilateral elements, featuring four quadrature points each, is taken into account as a reference. The macroscale stress state predicted by the finite element-based simulation reads

$$\boldsymbol{\sigma}^{\mathrm{FE}}_{\mathrm{M}} \approx 1216.6094\,\mathrm{MPa}\,\vec{e}_1 \otimes \vec{e}_1 + 515.3692\,\mathrm{MPa}\,\vec{e}_2 \otimes \vec{e}_2 \quad . \tag{62}$$

For the particular boundary value problem and the set of numerical control parameters chosen, the same number of iterations until convergence is required for the classical, non-adaptive FFT scheme and the wavelet-enhanced scheme with $\epsilon_W = 10^{-3}$ and $\epsilon_W = 10^{-4}$, respectively. However, it can be observed in Figure 13(a) that the convergence rate decreases with increasing values of refinement tolerance ϵ_W. This effect can be attributed to the wavelet approximation of the stress field as further analysed in Remark 2.

Clearly, a significant decrease in the number of material model evaluations with increasing values of the refinement tolerance is observed in Figure 13(b), whereas a similar level of accuracy in the prediction of the macroscale stresses is achieved in all simulations. The gain in computational efficiency results from the automatic activation of grid points in regions where significant changes in the solution profile occur. This is exemplified in Figure 14 where the active grid points are shown for various iteration steps and values of the refinement tolerance. The activation of grid points is based on the iterative values of the stress field. For the converged state, the stress and strain fields of the reference finite element simulation are provided in Figure 15 and those of the (wavelet-enhanced) FFT scheme are provided in Figure 16 and in Appendix C. In particular, it is observed that the wavelet approximation reproduces the non-physical oscillations that are inherent to the Moulinec-Suquet discretisation of a unit cell featuring weak discontinuities. This observation suggests that the gain in computational efficiency can further be increased by taking into account an Eshelby-Green operator associated with a more elaborated discretisation, e.g. of staggered grid-type [35, 21]. Against this background, Section 5.2.2 focuses on simulation results that are based on the Eshelby-Green operator derived in Section 3.2 that takes the underlying wavelet discretisation of the stress field into account.

Remark 2 (Shear loading and convergence rates). In this remark, additional simulation results focusing on the influence of the hierarchical wavelet-approximation on the convergence rate of the fixed-point iteration scheme are studied. To this end, the unit cell of Section 5.2.1 is subjected to shear loading, i.e. an average macroscale strain

$$\boldsymbol{\varepsilon}_M = 0.005\ [\vec{e}_1 \otimes \vec{e}_2 + \vec{e}_2 \otimes \vec{e}_1] \tag{63}$$

is prescribed in a single load step, giving rise to the macroscale stresses

$$\boldsymbol{\sigma}_M^{FE} \approx 689.5049\,\text{MPa}\ [\vec{e}_1 \otimes \vec{e}_2 + \vec{e}_2 \otimes \vec{e}_1] \quad . \tag{64}$$

For the same set of numerical parameters used in Section 5.2.1, the convergence rate, the number of material model evaluations and the accuracy of the macroscale stresses are provided in Figure 17. It can be observed that the calculation with refinement tolerance $\epsilon_W = 10^{-3}$ struggles to converge for the given set of numerical parameters (i.e. for convergence tolerance $\epsilon_F = 10^{-3}$) and requires almost twice the amount of iterations until convergence compared

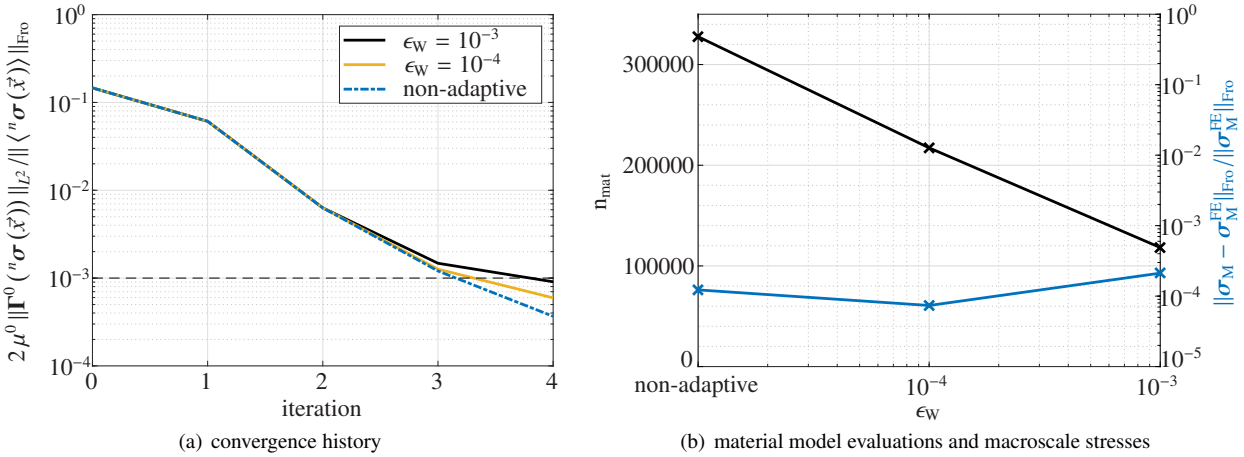

(a) convergence history

(b) material model evaluations and macroscale stresses

Figure 13: Convergence history, number of material model evaluations and error in macroscale stresses as a function of refinement tolerance ϵ_W for the two-dimensional tension problem discussed in Section 5.2.1 and sketched in Figure 12. The simulations are based on the original Eshelby-Green operator (associated with the Moulinec-Suquet discretisation). The convergence tolerance $\epsilon_F = 10^{-3}$ is indicated by a dashed line in a).

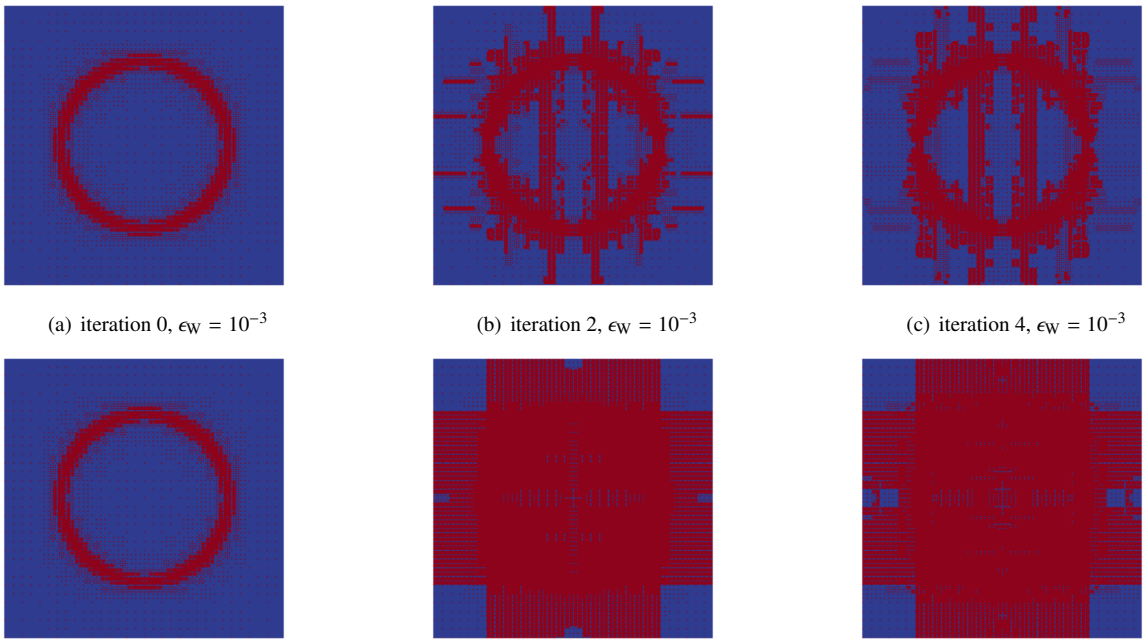

(a) iteration 0, $\epsilon_W = 10^{-3}$ (b) iteration 2, $\epsilon_W = 10^{-3}$ (c) iteration 4, $\epsilon_W = 10^{-3}$

(d) iteration 0, $\epsilon_W = 10^{-4}$ (e) iteration 2, $\epsilon_W = 10^{-4}$ (f) iteration 4, $\epsilon_W = 10^{-4}$

Figure 14: Activity of grid points in the tension problem of the unit cell shown in Figure 12 for different iteration steps and values of the refinement tolerance ϵ_W. The simulations are based on the original Eshelby-Green operator associated with the Moulinec-Suquet discretisation. Active grid points are marked in red colour, inactive grid points in blue colour.

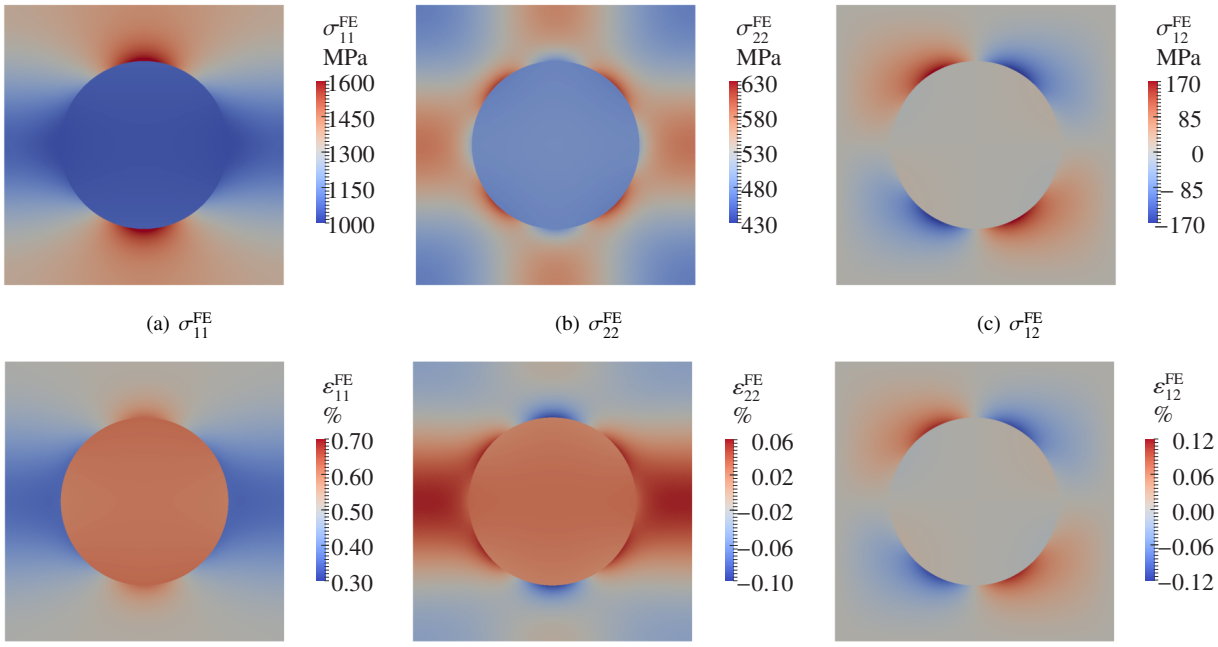

(a) σ_{11}^{FE} (b) σ_{22}^{FE} (c) σ_{12}^{FE}

(d) ε_{11}^{FE} (e) ε_{22}^{FE} (f) ε_{12}^{FE}

Figure 15: Microscale stress and strain fields for the boundary value problem according to Figure 12 and tensile loading, predicted by the reference finite element calculation with a geometrically conforming discretisation.

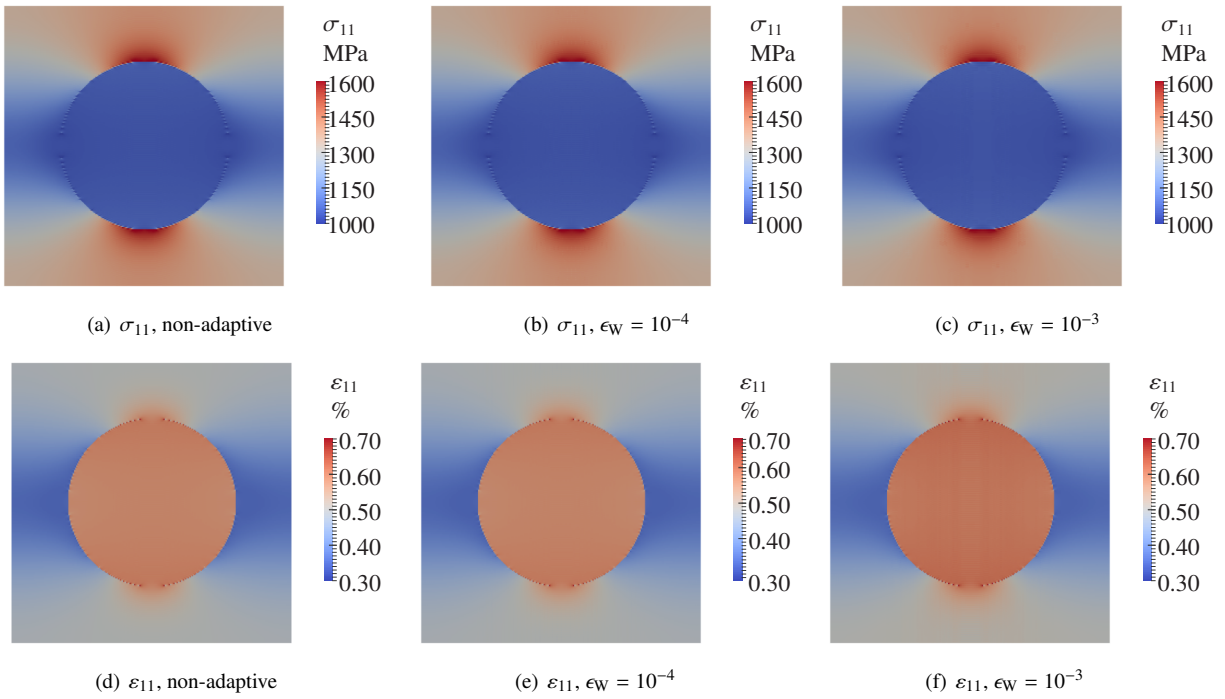

(a) σ_{11}, non-adaptive (b) σ_{11}, $\epsilon_W = 10^{-4}$ (c) σ_{11}, $\epsilon_W = 10^{-3}$

(d) ε_{11}, non-adaptive (e) ε_{11}, $\epsilon_W = 10^{-4}$ (f) ε_{11}, $\epsilon_W = 10^{-3}$

Figure 16: 11-components of the microscale stress and strain fields for the boundary value problem according to Figure 12 and tensile loading, predicted by a wavelet-enhanced FFT-based solution approach. The simulations are based on the original Eshelby-Green operator associated with the Moulinec-Suquet discretisation.

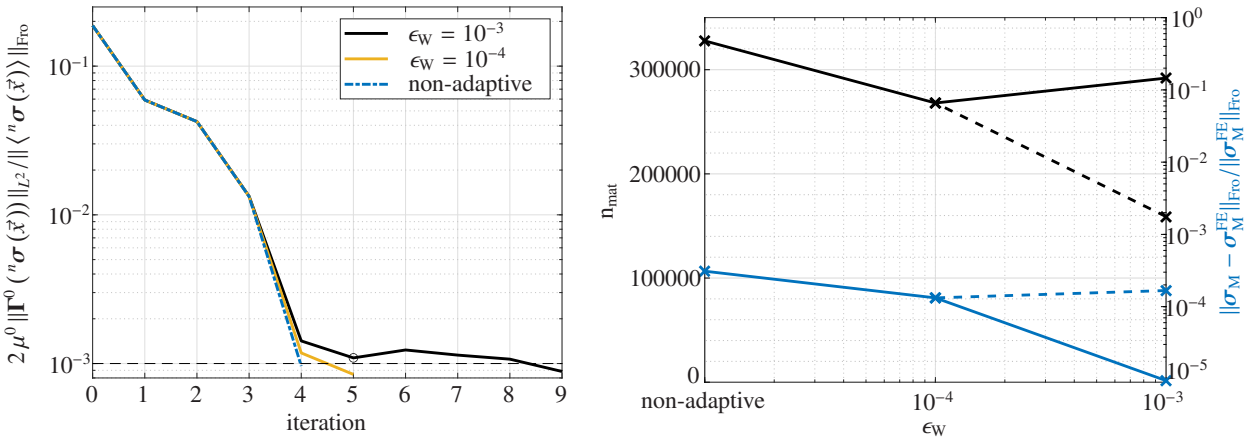

(a) convergence history (b) material model evaluations and macroscale stresses

Figure 17: Convergence history, number of material model evaluations and error in macroscale stresses as a function of refinement tolerance ϵ_W for the two-dimensional shear problem discussed in Remark 2 and sketched out in Figure 12. Solid lines in b) represent simulation results with $\epsilon_F = 10^{-3}$, dashed lines represent simulation results with $\epsilon_F = 1.1 * 10^{-3}$. The simulation with $\epsilon_W = 10^{-3}$ met the convergence tolerance $\epsilon_F = 10^{-3}$ after 9 iterations and the convergence tolerance $\epsilon_F = 1.1 * 10^{-3}$ after 5 iterations, as highlighted by the circular marker in a). The convergence tolerance $\epsilon_F = 10^{-3}$ is indicated by a dashed horizontal line in a). The simulations are based on the original Eshelby-Green operator associated with the Moulinec-Suquet discretisation.

with a non-adaptive scheme. Nevertheless, a modest reduction in the overall number of material model evaluations of approx. 11% is still achieved. When slightly changing the convergence tolerance to $\epsilon_F = 1.1 * 10^{-3}$, the gain in computational efficiency can further be increased to approx. 51% (dashed lines in Figure 17(b)) since the number

of required fixed-point iterations decreases to 5 (circular marker in Figure 17(a)). The macroscale stress tensor is predicted within the same level of accuracy in all simulations as shown in Figure 17(b).

5.2.2. Wavelet discretisation-based Eshelby-Green operator

In Section 5.2.1 it was shown that the proposed wavelet-based scheme can be used to enhance classic FFT-based solution approaches for microscale boundary value problems as to significantly reduce the computational effort in terms of material model evaluations. Yet, it is noted that the underlying wavelet discretisation was not accounted for in the particular structure of the Eshelby-Green operator (i.e. the classic Eshelby-Green operator associated with a Moulinec-Suquet discretisation of the field variables was used). In this section, focus lies on the influence of the Eshelby-Green operator on the simulation results. To this end, additional simulation results that are based on the Eshelby-Green operator associated with a wavelet discretisation (with $\widehat{\boldsymbol{\Gamma}^{j0}}\left(\vec{\vec{\xi}}_{\mathcal{B}}\right) = \mathbf{0}\ \forall\ \vec{\vec{\xi}}_{\mathcal{B}} \neq \vec{\vec{0}}$) as derived in Section 3.2 are considered. Note that almost the same convergence rate and activation of grid points is observed in simulations that alternatively assume $\widehat{\boldsymbol{\Gamma}^{j0}}\left(\vec{\vec{\xi}}_{\mathcal{B}}\right) = \left[\mathbf{E}^{0}\right]^{-1}\ \forall\ \vec{\vec{\xi}}_{\mathcal{B}} \neq \vec{\vec{0}}$.

Focusing on the tension problem introduced in Section 5.2.1, the influence of the particular choice of the Eshelby-Green operator on the convergence rate is small with almost the same accuracy of the macroscale stresses being achieved, see Figures 18(a) and 18(b). However, significant differences in the overall number of material model evaluations are observed. Whereas 118260 (for $\epsilon_{\mathrm{W}} = 10^{-3}$) and 217248 (for $\epsilon_{\mathrm{W}} = 10^{-4}$) material model evaluations were required in the simulations using a Moulinec-Suquet discretisation-based Eshelby-Green operator, only 52384 (for $\epsilon_{\mathrm{W}} = 10^{-3}$) and 90880 (for $\epsilon_{\mathrm{W}} = 10^{-4}$) material model evaluations are required when the underlying wavelet discretisation is taken into account. Thus, a significant additional gain in computational efficiency with regard to the number of material model evaluations is achieved. Compared to the 327680 material model evaluations required in the non-adaptive scheme, the number of material model evaluations is reduced by 72% for $\epsilon_{\mathrm{W}} = 10^{-4}$ and 84% for $\epsilon_{\mathrm{W}} = 10^{-3}$.

The additional gain in computational efficiency is due to the different activation of grid points in each fixed-point iteration step as shown in Figure 19. In particular, by comparing the simulation results shown in Figure 14 with those provided in Figure 19 it is apparent that significantly less grid points are activated "at a distance" from the material interface, e.g. close to the centre of the specimen. In other words, a significantly stronger localisation of the active grid points in the vicinity of the material interfaces is observed when the underlying wavelet discretisation is accounted for in the Eshelby-Green operator.

The microscale stress and strain fields in the converged state are additionally provided in Figure 20 and in Appendix C. Compared with their counterparts from Section 5.2.1, and as expected in virtue of the simulation results

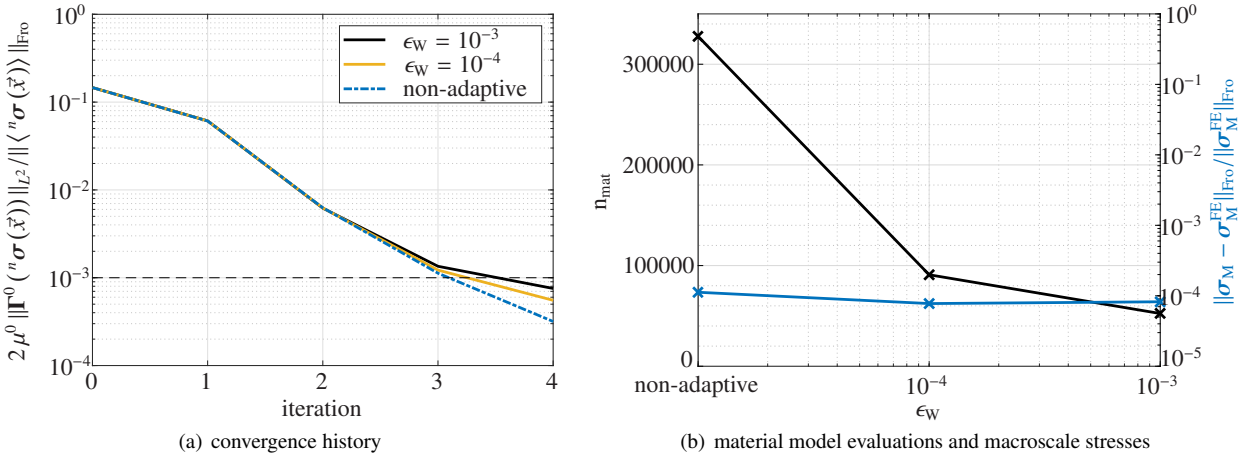

(a) convergence history

(b) material model evaluations and macroscale stresses

Figure 18: Convergence history, number of material model evaluations and error in macroscale stresses as a function of refinement tolerance ϵ_{W} for the two-dimensional tension problem discussed in Section 5.2.2 and sketched out in Figure 12. The simulations are based on an Eshelby-Green operator associated with a wavelet discretisation. The convergence tolerance $\epsilon_{\mathrm{F}} = 10^{-3}$ is indicated by a dashed line in a).

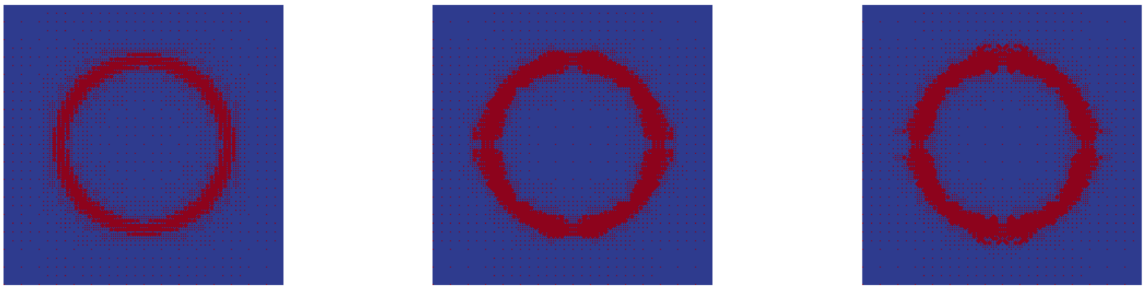

(a) iteration 0, $\epsilon_W = 10^{-3}$ (b) iteration 2, $\epsilon_W = 10^{-3}$ (c) iteration 4, $\epsilon_W = 10^{-3}$

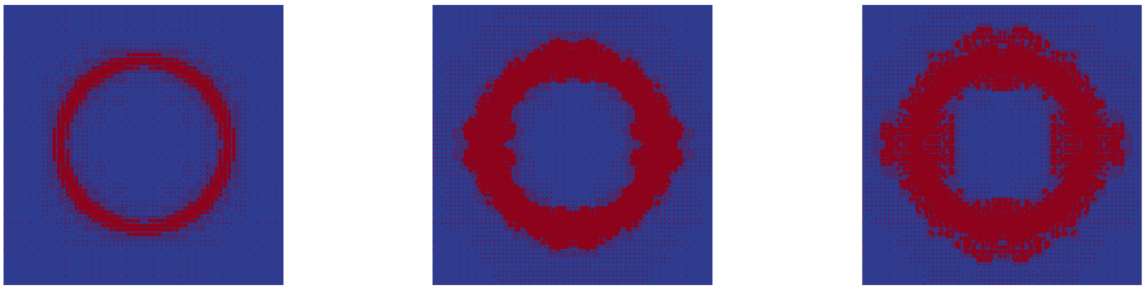

(d) iteration 0, $\epsilon_W = 10^{-4}$ (e) iteration 2, $\epsilon_W = 10^{-4}$ (f) iteration 4, $\epsilon_W = 10^{-4}$

Figure 19: Activity of grid points in the tension problem of the unit cell shown in Figure 12 for different iteration steps and values of the refinement tolerance ϵ_W. The simulations are based on the Eshelby-Green operator associated with the wavelet discretisation. Active grid points are marked in red colour inactive grid points in blue colour.

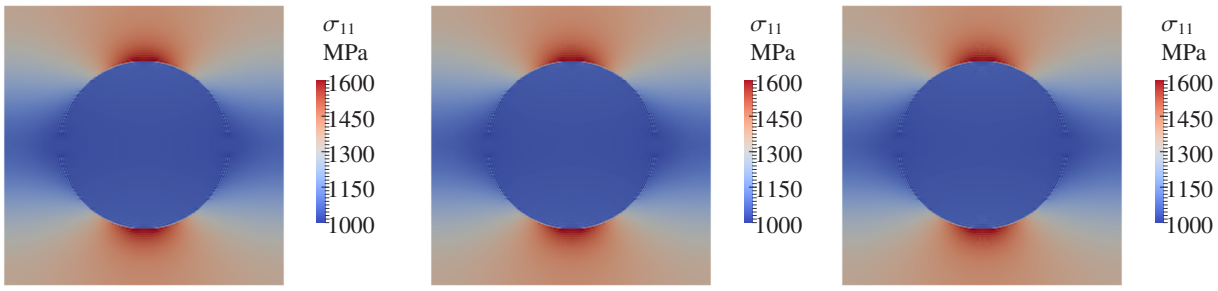

(a) σ_{11}, non-adaptive (b) σ_{11}, $\epsilon_W = 10^{-4}$ (c) σ_{11}, $\epsilon_W = 10^{-3}$

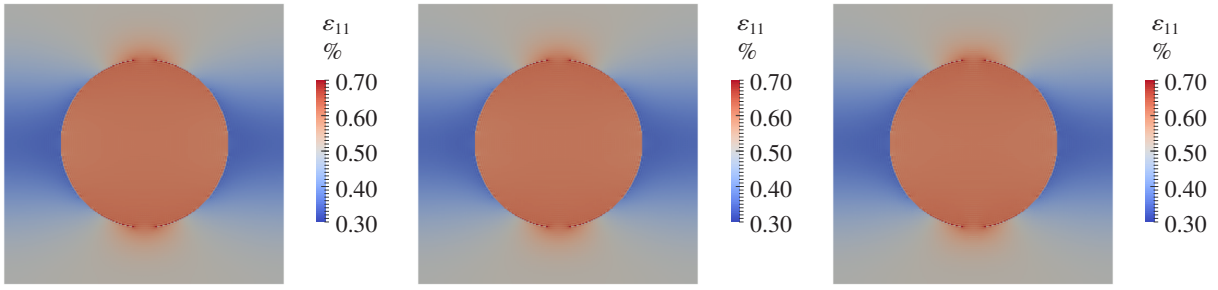

(d) ε_{11}, non-adaptive (e) ε_{11}, $\epsilon_W = 10^{-4}$ (f) ε_{11}, $\epsilon_W = 10^{-3}$

Figure 20: 11-components of the microscale stress and strain fields for the boundary value problem according to Figure 12 and tensile loading, predicted by a wavelet-enhanced FFT-based solution approach. The simulations are based on the Eshelby-Green operator associated with the wavelet discretisation.

for different Eshelby-Green operators discussed in, e.g., [21], somewhat different oscillations are observed when comparing for instance Figure 16(a) and Figure 20(a).

Remark 3 (Shear loading and convergence rates). Consistent with the tension problem in Section 5.2.2, the same tendencies are observed when considering the shear problem defined in Remark 2. Almost the same convergence rates can be noticed in Figures 17(a) and 21(a), and the macroscale stresses are for both cases predicted with a reasonable accuracy, cf. Figures 17(b) and 21(b). However, when using a Moulinec-Suquet discretisation-based Eshelby-Green operator 291956 (for $\epsilon_W = 10^{-3}$) and 268056 (for $\epsilon_W = 10^{-4}$) material model evaluations are required as opposed to the 138744 (for $\epsilon_W = 10^{-3}$) and 146368 (for $\epsilon_W = 10^{-4}$) material model evaluations that are required when accounting for the underlying wavelet discretisation in the Eshelby-Green operator.

By slightly modifying the convergence tolerance, the required number of material model evaluations can further be reduced to 78376 (for $\epsilon_W = 10^{-3}$ with $\epsilon_F = 1.15 * 10^{-3}$) such that an overall reduction of about 76% as compared to a non-adaptive scheme is achieved.

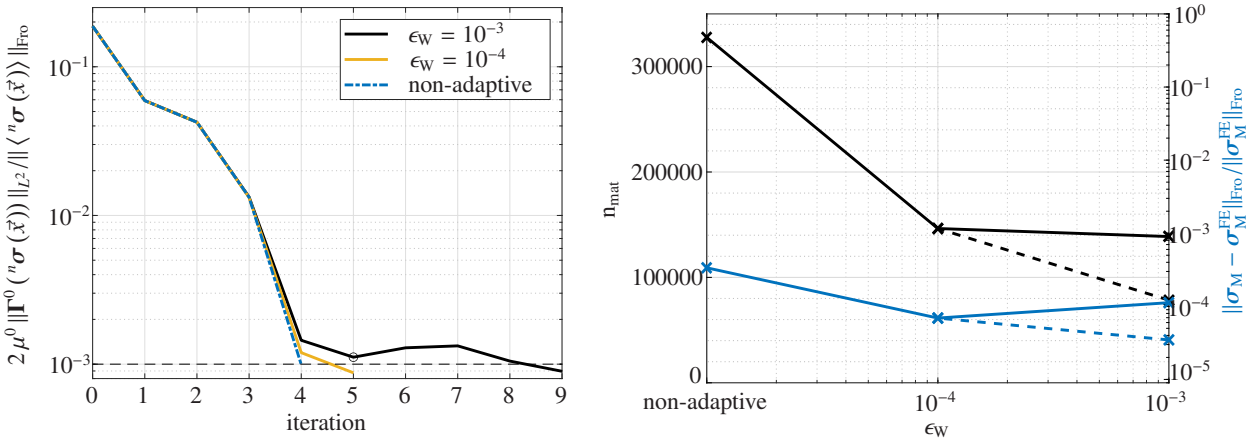

(a) convergence history

(b) material model evaluations and macroscale stresses

Figure 21: Convergence history, number of material model evaluations and error in the macroscale stress as a function of the refinement tolerance ϵ_W for the two-dimensional shear problem sketched in Figure 12. Solid lines in b) represent simulation results with $\epsilon_F = 10^{-3}$, dashed lines represent simulation results with $\epsilon_F = 1.15 * 10^{-3}$. The simulation with $\epsilon_W = 10^{-5}$ met the convergence tolerance $\epsilon_F = 10^{-3}$ after 9 iterations and the convergence tolerance $\epsilon_F = 1.15 * 10^{-3}$ after 5 iterations, as highlighted by the circular marker in a). The convergence tolerance $\epsilon_F = 10^{-3}$ is indicated by a dashed horizontal line in a). The simulations are based on the Eshelby-Green operator associated with the wavelet discretisation.

6. Concluding remarks

In this contribution, an adaptive hierarchical FFT-based approach for the efficient solution of microscale boundary value problems has been proposed. The formulation makes use of the natural hierarchy and adaptivity of wavelet-based approaches to adapt the computational grid to the solution profile and to significantly reduce the number of material model evaluations. To this end, the stress field was represented with respect to a wavelet basis and higher level stress approximations were successively derived by making use of wavelet synthesis operations. It was shown that the additional computational effort associated with the wavelet transforms is (almost) negligible compared to the numerical effort associated with the evaluation of non-linear history-dependent material models. Moreover, focusing on the solution of the Lippmann-Schwinger equation, a representation of the Eshelby-Green operator in Fourier space was derived that is consistent with the underlying wavelet discretisation.

In a first step, the proposed formulation was applied to representative one-dimensional boundary value problems for which analytical solutions serve as a reference. In particular, unit cells featuring sharp material interfaces and smooth material interphases as prototype problems, revealing significant local changes in the solution profile as frequently encountered in continuum mechanics applications, were studied. In both cases, the computational grid was

adapted to the solution profile – i.e. based on the proposed refinement criterion, significant grid-refinements were observed in the vicinity of the material interfaces and interphases, respectively. For the one-dimensional boundary value problems studied, the targeted activation of grid points in the hierarchical adaptive scheme eventually gave rise to a large reduction of up to 95% in the number material model evaluations while maintaining reasonable levels of accuracy.

In a second step, focus was laid on a rectangular two-dimensional unit cell featuring a circular inclusion. The unit cell was subjected to different average strains and the overall accuracy and the number of material model evaluations were analysed for different refinement tolerances. The influence of the particular form of the Eshelby-Green operator was thereby also studied. In agreement with the one-dimensional simulation results, significant reductions in the number of material model evaluations of up to 84% were observed while maintaining reasonable levels of accuracy. This remarkable gain in computational efficiency was again achieved by an automatic localised activation of grid points. In addition, it was shown that the gain in computational efficiency compared with a Moulinec-Suquet discretisation can further be increased by accounting for the underlying wavelet discretisation in the structure of the Eshelby-Green operator.

The enhancement of a classical FFT-based solution approach to microscale boundary value problems by making use of the multiresolution properties of wavelets has been demonstrated in the present contribution. The results are promising since the intrinsic hierarchical structure of the underlying wavelet discretisation naturally gave rise to grid refinement criteria. In contrast to classical FFT-based solution approaches that intrinsically rely on a regular grid with constant spacing, it was shown that the proposed wavelet-enhanced approach adequately resolves small-scale features while preserving a rather coarse discretisation in the remainder of the solution domain. By significantly reducing the overall number of material model evaluations, a notable gain in computational efficiency is achieved. Since the proposed wavelet-based approach naturally adapts the grid to the solution profile (in the sense that changes in the solution profile trigger local grid refinements) it seems particularly suitable for the simulation of microstructures that include evolving (possibly localised) features such as plastic deformation zones. The application to such microstructures, including associated wavelet-based mapping algorithms for state variables, will be the focus of future work.

Appendix A. Derivation of one-dimensional Lippmann-Schwinger equation

In line with the derivations in [24, 25], one-dimensional versions of the Lippmann-Schwinger equation are derived in this appendix. To this end, the auxiliary boundary value problem

$$E^0 \varepsilon^*(x) + \tau(x) = \sigma(x) \quad \forall x \in \mathcal{B} \quad , \tag{A.1a}$$

$$\nabla \cdot \sigma(x) = 0 \qquad \forall x \in \mathcal{B} \quad , \quad \omega(x^-) = \omega(x^+) , \quad \sigma(x^-) = \sigma(x^+) \tag{A.1b}$$

with x^+ and x^- denoting points at opposing parts of $\partial\mathcal{B}$, is introduced by considering a reference material with material constant E^0 and polarisation stresses $\tau(x)$. In frequency space, the set of equations (A.1) takes the form

$$\mathrm{i}\,\xi_{\mathcal{B}} \left[E^0 \widehat{\varepsilon^*}(\xi_{\mathcal{B}}) + \widehat{\tau}(\xi_{\mathcal{B}}) \right] = 0 \quad . \tag{A.2}$$

Together with the vanishing mean condition on the strain fluctuations, $\langle \varepsilon^* \rangle = 0$, (A.2) yields the Fourier and real space representations

$$\widehat{\varepsilon^*}(\xi_{\mathcal{B}}) = -\widehat{\Gamma^0}(\xi_{\mathcal{B}})\, \widehat{\tau}(\xi_{\mathcal{B}}) \quad \forall \xi_{\mathcal{B}} \neq 0 \quad , \quad \widehat{\varepsilon^*}(0) = 0 \tag{A.3a}$$

$$\varepsilon^*(x) = -\Gamma^0(\tau(x)) \qquad \forall x \in \mathcal{B} \tag{A.3b}$$

of the one-dimensional Lippmann-Schwinger equation in terms of the Eshelby–Green operator

$$\widehat{\Gamma^0}(\xi_{\mathcal{B}}) = \left[E^0 \right]^{-1} \forall \xi_{\mathcal{B}} \neq 0 \quad , \quad \widehat{\Gamma^0}(\xi_{\mathcal{B}}) = 0 \quad . \tag{A.4}$$

Moreover, by invoking the kinematic relation

$$\varepsilon(x) = \varepsilon^*(x) + \varepsilon_{\mathrm{M}} \quad , \quad \varepsilon^*(x) = \nabla\omega(x) \quad , \quad \langle \varepsilon \rangle = \varepsilon_{\mathrm{M}} \tag{A.5}$$

one arrives at the equivalent representation of (A.3) in terms of the strain field

$$\widehat{\varepsilon}(\xi_{\mathcal{B}}) = -\widehat{\Gamma^0}(\xi_{\mathcal{B}})\,\widehat{\tau}(\xi_{\mathcal{B}}) \qquad \forall \xi_{\mathcal{B}} \neq 0 \quad , \quad \widehat{\varepsilon}(0) = \varepsilon_{\mathrm{M}} \tag{A.6a}$$

$$\varepsilon(x) = -\Gamma^0(\tau(x)) + \varepsilon_{\mathrm{M}} \qquad \forall x \in \mathcal{B} \tag{A.6b}$$

By making use of (A.1a) and by observing that

$$\varepsilon^*(x) = \Gamma^0\left(E^0\,\varepsilon^*(x)\right) \tag{A.7}$$

holds, (A.6) may further be simplified and motivates the fixed-point-type basic scheme

$$^{n+1}\varepsilon(x) = {}^{n}\varepsilon(x) - \Gamma^0({}^{n}\sigma(x)) \quad . \tag{A.8}$$

Appendix B. Treatment of critical frequencies

In addition to the simulation results for material interfaces and material interphases discussed in Section 5.1.1 and Section 5.1.2, complementary simulation results for wavelet-based discretisations and the particular choice $\widehat{\Gamma^{j0}}\left(\frac{\pi w^j}{L}\right) =$

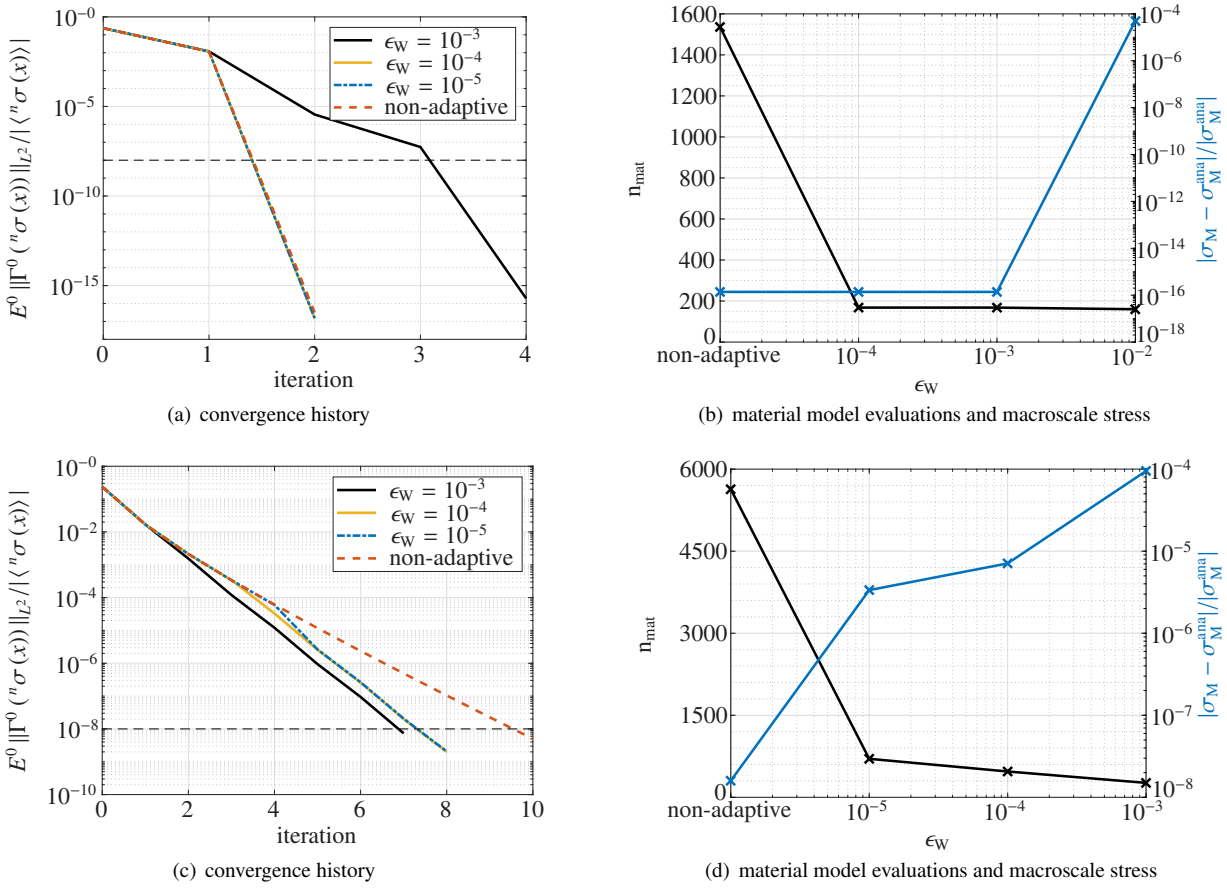

(a) convergence history

(b) material model evaluations and macroscale stress

(c) convergence history

(d) material model evaluations and macroscale stress

Figure B.22: Convergence history, number of material model evaluations $\mathrm{n_{mat}}$ and accuracy of macroscale stresses as a function of refinement tolerance ϵ_{W} for a wavelet-based discretisation with $\widehat{\Gamma^{j0}}\left(\frac{\pi w^j}{L}\right) = 0$. Complementary simulation results for the material interface problem and the material interphase problem according to Section 5.1.1 and Section 5.1.2 are provided in a)-b) and c)-d), respectively. The convergence tolerance $\epsilon_{\mathrm{F}} = 10^{-8}$ is indicated by dashed lines in a) and c).

0 are provided in Figure B.22. In agreement with observations made on finite difference scheme-based Eshelby-Green operators [34], it is observed that the convergence rate, the number of material model evaluations and the accuracy of the macroscale stresses are (almost) not influenced by the particular choice of the Eshelby-Green operator at the critical frequency.

Appendix C. Supplementary simulation results

In this appendix, supplementary two-dimensional simulation results are provided. The 22- and 12-components of the microscale stress and strain fields as predicted by the wavelet-enhanced FFT-based approach using a classical Moulinec-Suquet discretisation and a wavelet-based discretisation are shown in Figures C.23 and C.24 and in Figures C.25 and C.26, respectively.

References

[1] K. Matouš, M. G. D. Geers, V. G. Kouznetsova, A. Gillman, A review of predictive nonlinear theories for multiscale modeling of heterogeneous materials, Journal of Computational Physics 330 (2017) 192–220. doi:10.1016/j.jcp.2016.10.070.

[2] P. M. Suquet, Local and global aspects in the mathematical theory of plasticity, in: A. Sawczuck, G. Bianchi (Eds.), Plasticity Today: Modelling, Methods and Applications, Springer Netherlands, Dordrecht, 1985, pp. 279–310.

[3] J. Renard, M. F. Marmonier, Etude de l'initiation de l'endommagement dans la matrice d'un matériau composite par une méthode d'homogénéisation, Aerospace Science and Technology (6) (1987) 43–51.

[4] C. Miehe, J. Schotte, J. Schröder, Computational micro-macro transitions and overall moduli in the analysis of polycrystals at large strains, Computational Materials Science 16 (1) (1999) 372–382. doi:10.1016/S0927-0256(99)00080-4.

[5] F. Feyel, J.-L. Chaboche, FE^2 multiscale approach for modelling the elastoviscoplastic behaviour of long fibre SiC/Ti composite materials, Computer Methods in Applied Mechanics and Engineering 183 (3) (2000) 309–330. doi:10.1016/S0045-7825(99)00224-8.

[6] V. G. Kouznetsova, W. A. M. Brekelmans, F. P. T. Baaijens, An approach to micro-macro modeling of heterogeneous materials, Computational Mechanics 27 (1) (2001) 37–48. doi:10.1007/s004660000212.

[7] S. Ricker, J. Mergheim, P. Steinmann, R. Müller, A comparison of different approaches in the multi-scale computation of configurational forces, International Journal of Fracture 166 (2010) 203–214. doi:10.1007/s10704-010-9525-2.

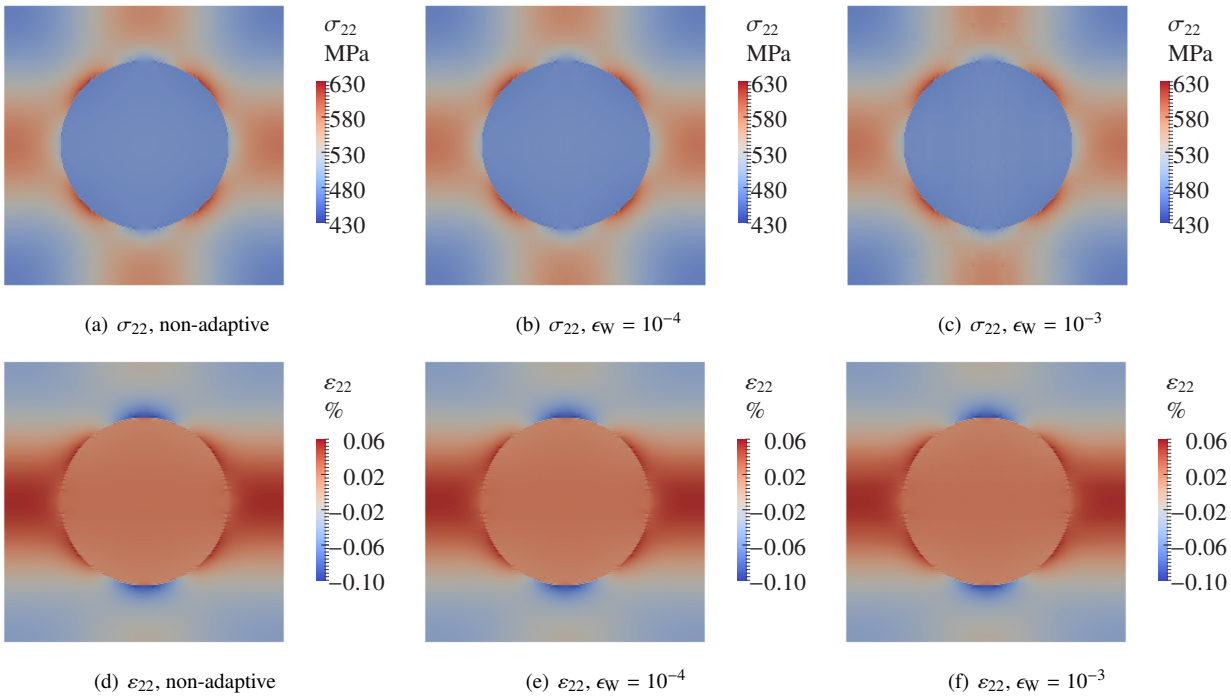

(a) σ_{22}, non-adaptive (b) σ_{22}, $\epsilon_W = 10^{-4}$ (c) σ_{22}, $\epsilon_W = 10^{-3}$

(d) ε_{22}, non-adaptive (e) ε_{22}, $\epsilon_W = 10^{-4}$ (f) ε_{22}, $\epsilon_W = 10^{-3}$

Figure C.23: 22-components of the microscale stress and strain fields for the boundary value problem according to Figure 12 and tensile loading, predicted by a wavelet-enhanced FFT-based solution approach. The simulations are based on the original Eshelby-Green operator associated with the Moulinec-Suquet discretisation.

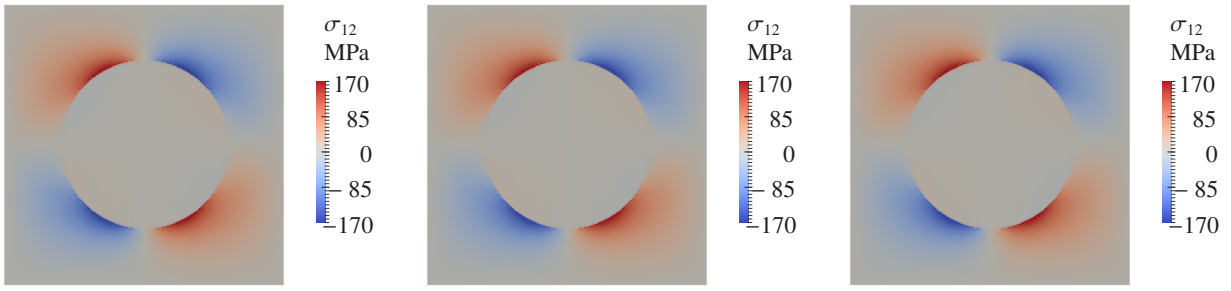

(a) σ_{12}, non-adaptive (b) σ_{12}, $\epsilon_W = 10^{-4}$ (c) σ_{12}, $\epsilon_W = 10^{-3}$

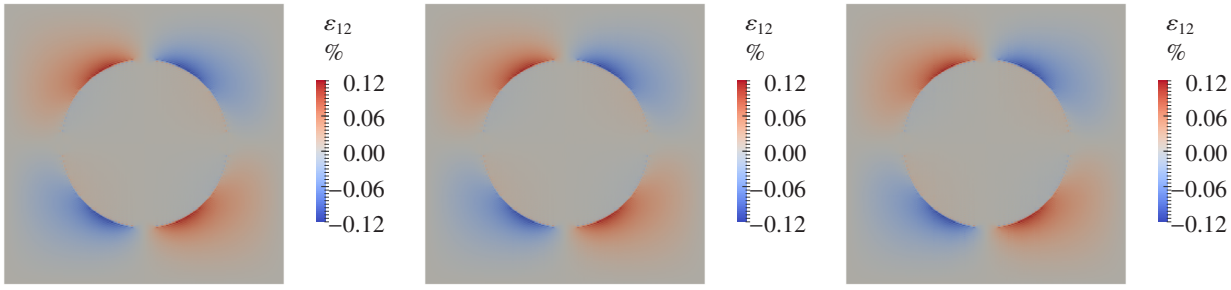

(d) ε_{12}, non-adaptive (e) ε_{12}, $\epsilon_W = 10^{-4}$ (f) ε_{12}, $\epsilon_W = 10^{-3}$

Figure C.24: 12-components of the microscale stress and strain fields for the boundary value problem according to Figure 12 and tensile loading, predicted by a wavelet-enhanced FFT-based solution approach. The simulations are based on the original Eshelby-Green operator associated with the Moulinec-Suquet discretisation.

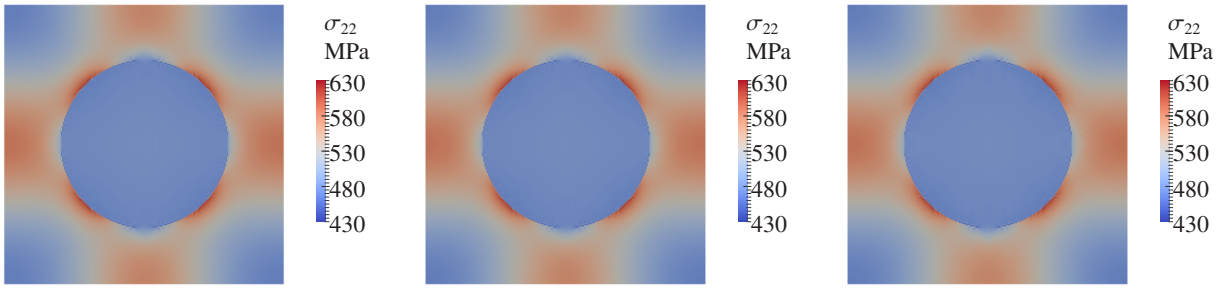

(a) σ_{22}, non-adaptive (b) σ_{22}, $\epsilon_W = 10^{-4}$ (c) σ_{22}, $\epsilon_W = 10^{-3}$

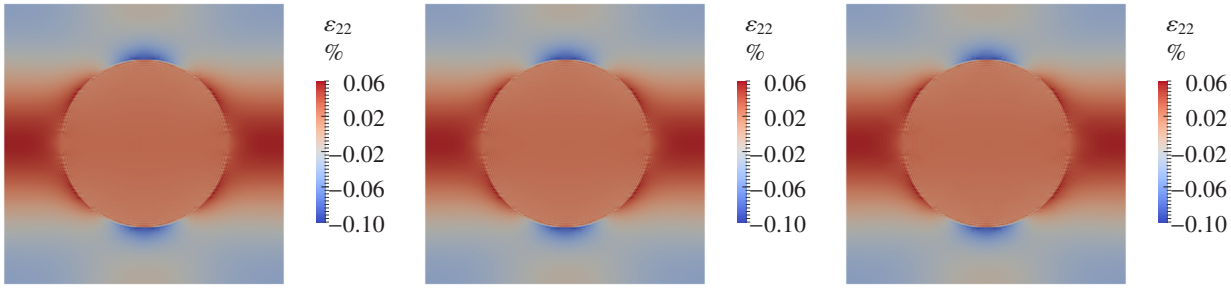

(d) ε_{22}, non-adaptive (e) ε_{22}, $\epsilon_W = 10^{-4}$ (f) ε_{22}, $\epsilon_W = 10^{-3}$

Figure C.25: 22-components of the microscale stress and strain fields for the boundary value problem according to Figure 12 and tensile loading, predicted by a wavelet-enhanced FFT-based solution approach. The simulations are based on the Eshelby-Green operator associated with the wavelet discretisation.

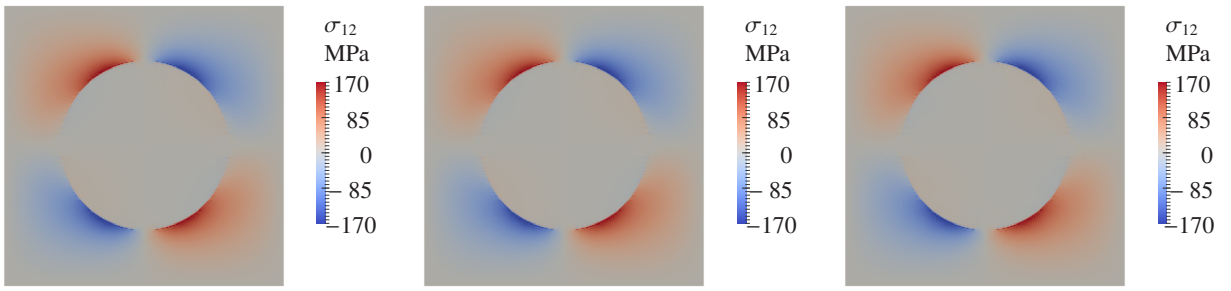

(a) σ_{12}, non-adaptive (b) σ_{12}, $\epsilon_W = 10^{-4}$ (c) σ_{12}, $\epsilon_W = 10^{-3}$

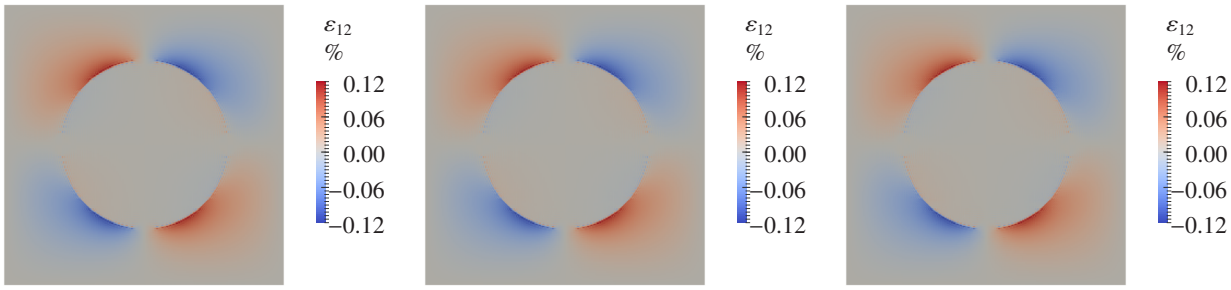

(d) ε_{12}, non-adaptive (e) ε_{12}, $\epsilon_W = 10^{-4}$ (f) ε_{12}, $\epsilon_W = 10^{-3}$

Figure C.26: 12-components of the microscale stress and strain fields for the boundary value problem according to Figure 12 and tensile loading, predicted by a wavelet-enhanced FFT-based solution approach. The simulations are based on the Eshelby-Green operator associated with the wavelet discretisation.

[8] E. W. C. Coenen, V. G. Kouznetsova, E. Bosco, M. G. D. Geers, A multi-scale approach to bridge microscale damage and macroscale failure: a nested computational homogenization-localization framework, International Journal of Fracture 178 (2012) 157–178. doi:10.1007/s10704-012-9765-4.

[9] A. Javili, P. Steinmann, J. Mosler, Micro-to-macro transition accounting for general imperfect interfaces, Computer Methods in Applied Mechanics and Engineering 317 (2017) 274–317. doi:10.1016/j.cma.2016.12.025.

[10] I. Özdemir, W. A. M. Brekelmans, M. G. D. Geers, FE^2 computational homogenization for the thermo-mechanical analysis of heterogeneous solids, Computer Methods in Applied Mechanics and Engineering 198 (3) (2008) 602–613. doi:10.1016/j.cma.2008.09.008.

[11] İ. Temizer, P. Wriggers, Homogenization in finite thermoelasticity, Journal of the Mechanics and Physics of Solids 59 (2) (2011) 344–372. doi:10.1016/j.jmps.2010.10.004.

[12] A. Sengupta, P. Papadopoulos, R. L. Taylor, A multiscale finite element method for modeling fully coupled thermomechanical problems in solids, International Journal for Numerical Methods in Engineering 91 (13) (2012) 1386–1405. doi:10.1002/nme.4320.

[13] R. Berthelsen, R. Denzer, P. Oppermann, A. Menzel, Computational homogenisation for thermoviscoplasticity: Application to thermally sprayed coatings, Computational Mechanics 60 (5) (2017) 739–766. doi:10.1007/s00466-017-1436-x.

[14] R. Berthelsen, A. Menzel, Computational homogenisation of thermo-viscoplastic composites: Large strain formulation and weak micro-periodicity, Computer Methods in Applied Mechanics and Engineering 348 (2019) 575–603. doi:10.1016/j.cma.2018.12.032.

[15] T. Kaiser, A. Menzel, An electro-mechanically coupled computational multiscale formulation for electrical conductors, Archive of Applied Mechanics 91 (2021) 1509–1526. doi:10.1007/s00419-020-01837-6.

[16] T. Kaiser, A. Menzel, A finite deformation electro-mechanically coupled computational multiscale formulation for electrical conductors, Acta Mechanica, Available Online (2021). doi:10.1007/s00707-021-03005-5.

[17] J. Schröder, Derivation of the localization and homogenization conditions for electro-mechanically coupled problems, Computational Materials Science 46 (3) (2009) 595–599. doi:10.1016/j.commatsci.2009.03.035.

[18] M. Khalaquzzaman, B.-X. Xu, S. Ricker, R. Müller, Computational homogenization of piezoelectric materials using FE^2 to determine configurational forces, Technische Mechanik 32 (1) (2012) 21–37.

[19] M.-A. Keip, P. Steinmann, J. Schröder, Two-scale computational homogenization of electro-elasticity at finite strains, Computer Methods in Applied Mechanics and Engineering 278 (2014) 62–79. doi:10.1016/j.cma.2014.04.020.

[20] T. Kanit, S. Forest, I. Galliet, V. Mounoury, D. Jeulin, Determination of the size of the representative volume element for random composites: statistical and numerical approach, International Journal of Solids and Structures 40 (13) (2003) 3647–3679. doi:10.1016/S0020-7683(03)00143-4.

[21] M. Schneider, A review of nonlinear FFT-based computational homogenization methods, Acta Mechanica 232 (2021) 2051–2100. doi:10.1007/s00707-021-02962-1.

[22] C. Gierden, J. Kochmann, J. Waimann, B. Svendsen, S. Reese, A review of FE-FFT-based two-scale methods for computational modeling

of microstructure evolution and macroscopic material behavior, Archives of Computational Methods in Engineering 29 (2022) 4115–4135. doi:10.1007/s11831-022-09735-6.
[23] H. Moulinec, P. Suquet, A fast numerical method for computing the linear and nonlinear mechanical properties of composites, Comptes rendus de l'Académie des sciences. Série II, Mécanique, physique, chimie, astronomie 318 (11) (1994) 1417–1426.
[24] H. Moulinec, P. Suquet, A numerical method for computing the overall response of nonlinear composites with complex microstructure, Computer Methods in Applied Mechanics and Engineering 157 (1) (1998) 69–94. doi:10.1016/S0045-7825(97)00218-1.
[25] J. C. Michel, H. Moulinec, P. Suquet, Effective properties of composite materials with periodic microstructure: a computational approach, Computer Methods in Applied Mechanics and Engineering 172 (1) (1999) 109–143. doi:10.1016/S0045-7825(98)00227-8.
[26] M. Frigo, S. Johnson, The design and implementation of FFTW3, Proceedings of the IEEE 93 (2) (2005) 216–231. doi:10.1109/JPROC.2004.840301.
[27] L. Dalcin, M. Mortensen, D. E. Keyes, Fast parallel multidimensional FFT using advanced MPI, Journal of Parallel and Distributed Computing 128 (2019) 137–150. doi:10.1016/j.jpdc.2019.02.006.
[28] M. Schneider, On the Barzilai-Borwein basic scheme in FFT-based computational homogenization, International Journal for Numerical Methods in Engineering 118 (8) (2019) 482–494. doi:10.1002/nme.6023.
[29] J. Zeman, J. Vondřejc, J. Novák, I. Marek, Accelerating a fft-based solver for numerical homogenization of periodic media by conjugate gradients, Journal of Computational Physics 229 (21) (2010) 8065–8071. doi:10.1016/j.jcp.2010.07.010.
[30] J. C. Michel, H. Moulinec, P. Suquet, A computational scheme for linear and non-linear composites with arbitrary phase contrast, International Journal for Numerical Methods in Engineering 52 (1–2) (2001) 139–160. doi:10.1002/nme.275.
[31] V. Monchiet, G. Bonnet, A polarization-based FFT iterative scheme for computing the effective properties of elastic composites with arbitrary contrast, International Journal for Numerical Methods in Engineering 89 (11) (2012) 1419–1436. doi:https://doi.org/10.1002/nme.3295.
[32] M. Schneider, An FFT-based fast gradient method for elastic and inelastic unit cell homogenization problems, Computer Methods in Applied Mechanics and Engineering 315 (2017) 846–866. doi:10.1016/j.cma.2016.11.004.
[33] F. Willot, B. Abdallah, Y.-P. Pellegrini, Fourier-based schemes with modified green operator for computing the electrical response of heterogeneous media with accurate local fields, International Journal for Numerical Methods in Engineering 98 (7) (2014) 518–533. doi:10.1002/nme.4641.
[34] F. Willot, Fourier-based schemes for computing the mechanical response of composites with accurate local fields, Comptes Rendus Mécanique 343 (3) (2015) 232–245. doi:10.1016/j.crme.2014.12.005.
[35] M. Schneider, F. Ospald, M. Kabel, Computational homogenization of elasticity on a staggered grid, International Journal for Numerical Methods in Engineering 105 (9) (2016) 693–720. doi:10.1002/nme.5008.
[36] S. Lucarini, M. V. Upadhyay, J. Segurado, FFT based approaches in micromechanics: fundamentals, methods and applications, Modelling and Simulation in Materials Science and Engineering (2021). doi:10.1088/1361-651X/ac34e1.
[37] J. Morlet, G. Arens, E. Fourgeau, D. Glard, Wave propagation and sampling theory–Part I: Complex signal and scattering in multilayered media, Geophysics 47 (4) (1982) 203–221. doi:10.1190/1.1441328.
[38] M. Smith, T. Barnwell, Exact reconstruction techniques for tree-structured subband coders, IEEE Transactions on Acoustics, Speech, and Signal Processing 34 (3) (1986) 434–441. doi:10.1109/TASSP.1986.1164832.
[39] A. Grossmann, J. Morlet, T. Paul, Transforms associated to square integrable group representations. I. General results, Journal of Mathematical Physics 26 (10) (1985) 2473–2479. doi:10.1063/1.526761.
[40] S. G. Mallat, A theory for multiresolution signal decomposition: the wavelet representation, IEEE Transactions on Pattern Analysis and Machine Intelligence 11 (7) (1989) 674–693. doi:10.1109/34.192463.
[41] B. Li, X. Chen, Wavelet-based numerical analysis: A review and classification, Finite Elements in Analysis and Design 81 (2014) 14–31. doi:10.1016/j.finel.2013.11.001.
[42] J. R. Williams, K. Amaratunga, Introduction to wavelets in engineering, International Journal for Numerical Methods in Engineering 37 (14) (1994) 2365–2388. doi:10.1002/nme.1620371403.
[43] O. V. Vasilyev, C. Bowman, Second-generation wavelet collocation method for the solution of partial differential equations, Journal of Computational Physics 165 (2000) 660–693. doi:10.1006/jcph.2000.6638.
[44] C. Harnish, K. Matouš, D. Livescu, Adaptive wavelet algorithm for solving nonlinear initial-boundary value problems with error control, International Journal for Multiscale Computational Engineering 16 (1) (2018) 19–43. doi:10.1615/IntJMultCompEng.2018024915.
[45] C. Harnish, L. Dalessandro, K. Matouš, D. Livescu, A multiresolution adaptive wavelet method for nonlinear partial differential equations, International Journal for Multiscale Computational Engineering 19 (2) (2021) 29–37. doi:10.1615/IntJMultCompEng.2021039451.
[46] K. Amaratunga, J. R. Williams, Wavelet based Green's function approach to 2D PDEs, Engineering Computations 10 (1993) 349–367. doi:10.1108/eb023913.
[47] K. Amaratunga, J. R. Williams, S. Qian, J. Weiss, Wavelet-Galerkin solutions for one-dimensional partial differential equations, International Journal for Numerical Methods in Engineering 37 (16) (1994) 2703–2716. doi:10.1002/nme.1620371602.
[48] S. Jones, M. Legrand, The wavelet-Galerkin method for solving PDE's with spatially de-pendent variables, 19th International Congress on Sound and Vibration (ICSV19) (2012) 1–8.
[49] M. A. Christon, D. W. Roach, The numerical performance of wavelets for PDEs: the multi-scale finite element, Computational Mechanics 25 (2000) 230–244. doi:10.1007/s004660050472.
[50] J. E. Kim, G.-W. Jang, Y. Y. Kim, Adaptive multiscale wavelet-Galerkin analysis for plane elasticity problems and its applications to multiscale topology design optimization, International Journal of Solids and Structures 40 (23) (2003) 6473–6496. doi:10.1016/S0020-7683(03)00417-7.
[51] C. Harnish, L. Dalessandro, K. Matouš, D. Livescu, An adaptive wavelet method for nonlinear partial differential equations with applications to dynamic damage modeling, arXiv preprint (2022). doi:10.48550/arXiv.2209.12380.
[52] Y. Azdoud, S. Ghosh, Adaptive wavelet-enriched hierarchical finite element model for polycrystalline microstructures, Computer Methods in Applied Mechanics and Engineering 370 (2017) 337–360. doi:10.1016/j.cma.2017.04.018.
[53] Y. Azdoud, J. Cheng, S. Ghosh, Wavelet-enriched adaptive crystal plasticity finite element model for polycrystalline microstructures, Com-

puter Methods in Applied Mechanics and Engineering 327 (2017) 36–57. doi:10.1016/j.cma.2017.08.026.
[54] R. A. van Tuijl, C. Harnish, K. Matouš, J. J. C. Remmers, M. G. D. Geers, Wavelet based reduced order models for microstructural analyses, Computational Mechanics 63 (3) (2019) 535–554. doi:10.1007/s00466-018-1608-3.
[55] R. A. van Tuijl, J. J. C. Remmers, M. G. D. Geers, Multi-dimensional wavelet reduction for the homogenisation of microstructures, Computer Methods in Applied Mechanics and Engineering 359 (2020) 112652. doi:10.1016/j.cma.2019.112652.
[56] I. Daubechies, Ten Lectures on Wavelets, Society for Industrial and Applied Mathematics, Philadelphia, 1992. doi:10.1137/1.9781611970104.
[57] S. Goedecker, Wavelets and Their Application for the Solution of Partial Differential Equations in Physics, Presses Polytechniques et Universitaires Romandes, Lausanne, 1998.
[58] A. Cohen, Numerical Analysis of Wavelet Methods, Vol. 32 of Studies in Mathematics and Its Applications, Elsevier, 2003. doi:10.1016/S0168-2024(03)80495-2.
[59] P. Nickolas, Wavelets: A Student Guide, Australian Mathematical Society Lecture Series, Cambridge University Press, 2017. doi:10.1017/9781139644280.
[60] S. Goedecker, Wavelets and their application for the solution of Poisson's and Schrödinger's equation, in: J. Grotendorst, N. Attig, S. Blügel, D. Marx (Eds.), Multiscale Simulation Methods in Molecular Sciences, Institute for Advanced Simulation, Forschungszentrum Jülich, 2009, pp. 507–534.
[61] G. Deslauriers, S. Dubuc, Symmetric iterative interpolation processes, Constructive Approximation 5 (1989) 49–68. doi:10.1007/978-1-4899-6886-9_3.
[62] J. Barzilai, J. M. Borwein, Two-point step size gradient methods, IMA Journal of Numerical Analysis 8 (1988) 141–148. doi:10.1093/imanum/8.1.141.
[63] J. C. Simo, T. J. R. Hughes, Computational Inelasticity, Springer, New York, 1998, Ch. 3 Integration Algorithms for Plasticity and Viscoplasticity, pp. 113–153. doi:10.1007/0-387-22763-6_3.

Declaration of interests

☒The authors declare that they have no known competing financial interests or personal relationships that could have appeared to influence the work reported in this paper.

☐The authors declare the following financial interests/personal relationships which may be considered as potential competing interests: